SAND2022-7014J

Friction Stir Welding and Self-Ion Irradiation Effects on Microstructure and Mechanical Properties Changes within Oxide Dispersion Strengthened Steel MA956

E. Getto*, M. Johnson, M. Maughan, N. Nathan, J. McMahan, B. Baker, K. Knipling, S. Briggs, K. Hattar, M.J. Swenson

*Corresponding author: Elizabeth Getto getto@usna.edu 590 Holloway Rd Annapolis MD 21402

Abstract:

The joining process for oxide dispersion strengthened (ODS) alloys remains a key challenge facing the nuclear community. The microstructure and mechanical properties were characterized in the base material and friction stir welded ODS MA956 irradiated with 5 MeV Fe^{++} ions from 400 to 500°C up to 25 dpa. Nanoindentation was performed to assess changes in hardness and yield stress, and the dispersed barrier hardening (DBH) model was applied to described results. A combination of scanning transmission electron microscopy (STEM) and atom probe tomography (APT) were used to assess evolution of the microstructure including dispersoids, network dislocations and dislocation loops, nanoclusters, and solid solution concentrations. Overall, softening was observed as a result of increased dose, which was exacerbated at 500°C. The formation and coarsening of new dispersoids was noted while nanoclusters tended to dissolve in the base material, and were not observed in the stir zone. Solute nanocluster evolution was identified as a primary driver of the changes in mechanical properties.

Keywords: radiation effects, MA956, friction stir welding, microstructure, nanoindentation

Highlights

- MA956 exhibited radiation induced softening with increased temperature and dose.
- Formation of nanoclusters in the base material influenced mechanical properties.
- New dispersoids formed in the stir zone after irradiation.
- Dispersed barrier hardening model used to understand role of microstructure on yield stress.

CRediT Author Statement
Elizabeth Getto: Project administration, Methodology, Investigation, Formal Analysis, Visualization, Writing-Original Draft, Writing-Review & Editing, Supervision, Funding acquisition
M. Johnson: Methodology, Formal Analysis, Writing- Original Draft
M. Maughan: Methodology, Writing-Review & Editing
Nicholas Nathan: Investigation, Writing-Review & Editing
Jack McMahan: Investigation, Writing- Review & Editing
Brad Baker: Methodology, Investigation, Review & Editing
Keith Knipling: Data curation, Investigation, Review & Editing
Samuel Briggs: Investigation, Review & Editing
K. Hattar: Investigation, Review & Editing
M.J. Swenson: Methodology, Formal Analysis, Visualization, Writing-Original Draft, Writing-Review & Editing, Supervision

1 Introduction

The behavior of structural materials under irradiation is a critical issue facing both the fourth generation (GenIV) and the small modular reactor communities. The latter have gained popularity due to their smaller capital costs, improved public perception, as well being easily deployed for humanitarian purposes to areas affected by natural disaster or remote areas where a traditional light water reactor would not be economical [1]. To support the industry, self-ion irradiations address some of the challenges with performing well controlled neutron irradiations to assess reactor structural materials. Since dose rates of up to 10^{-3} dpa/s can be achieved, many more experiments can be performed in a short amount of time without the residual radioactivity making systematic study much easier [2–4]. However, the limited penetration depth makes assessing the mechanical properties a challenge as the irradiated volume is small relative to traditional mechanical testing samples [5].

Oxide dispersion strengthened (ODS) steels have been shown to be radiation tolerant at high dose under neutron and ion radiation [6–8]. However, joining of ODS alloys is difficult, and negative effects on the microstructure is exacerbated by the deleterious effects of irradiation. A consolidated weld with acceptable mechanical properties is critical to deploying novel ODS materials in new reactor designs. Traditional fusion welding is unsuitable for ODS steels as ODS particles will melt or agglomerate during the welding process [9]. Friction stir welding (FSW) is a solid state welding technique, which could potentially minimize defects and adverse changes in the microstructure relative to other welding techniques [10–13]. The combination of friction stir welding and irradiation is a unique area with limited previous work [14–16] at reactor-relevant experimental conditions.

Friction stir welding has been shown to be very sensitive to initial conditions. With a pre-existing coarse grain structure, welding tends to cause dynamic re-crystallization [17–19]. With a fine-grained microstructure, the addition of welding tends to cause coarsening of the microstructure [10,16]. The dispersoids tended to coarsen with welding [12,17,20] though some authors noted little change [16]. This paper focused on the behavior of the dispersoids and nanoclusters in particular- a recent review by Wharry et al. [21] suggested two primary irradiation mechanisms including ballistic dissolution which destabilizes precipitates tending to lead to decreases in average diameter and number density but also a competing mechanism of radiation-enhanced diffusion . The balancing of these two mechanisms leads to Ostwald coarsening, where precipitates grow in size but decrease in number density due to material diffusing from the dissolved ppts to larger more stable sites. In this allow, previous results show Ostwald coarsening dominating the base material whereas radiation enhanced diffusion caused re-formation of dispersoids that were solutioned during the weld process [6,22,23].

Other than prior work from this research team on this particular alloy at high dose [6] and several welding conditions [22,23], we are aware of only one other combined irradiation and welding study at reactor-relevant temperatures. Guo et al. irradiated friction stir welded 12Cr-ODS steel [14]. The irradiated steel was welded in a friction stir machine (FSW-TS-08) with a W-Re pin tool. Welding direction was parallel to the rolling direction with a tool rotation speed of 150 rev·min^{-1} and traverse speed of 30 mm·min^{-1}. The ODS steel, both welded and base material, were irradiated with 3 MeV Au ions up to 2.7 dpa at 500^{o}C. After welding, the stir zone (SZ) exhibited uniform fine-grain structure (286±144 nm), attributed to dynamic recrystallization as the base material (BM) grains were quite large and elongated (775±306 nm). Dispersoids coarsened from 4.8 nm to 7.4 nm in the SZ with a large decrease in dispersoid number density from 1.43×10^{22} m^{-3} to 4.66×10^{20} m^{-3}. Decreased grain size across the weld resulted in an increase in nanoindentation-measured hardness. After irradiation, nanoindentation hardness values increased in the

BM (6.37 to 6.53 GPa), but decreased in the SZ (7.48 to 7.37 GPa). Voids were observed in the BM and heat affected zone but not in the SZ, suggesting that a decreased grain size was responsible for the increased radiation tolerance observed.

The present report is the first systematic study of the effects of irradiation at reactor-relevant conditions on the microstructures of friction stir welded material MA956 and the attendant effects on mechanical properties. Mechanical properties will be assessed with nanoindentation. The microstructure will be characterized using scanning transmission electron microscopy (STEM) and atom-probe tomography (APT), and these results are explained by utilizing the characterized microstructure as inputs into a dispersed barrier hardness model.

2 Material and Methods

The material studied was an un-recrystallized fine-grained MA956 steel plate, the composition of which is given in Table 1. The alloy was canned and extruded at 1100°C and hot rolled in three passes at 1100°C over 4 hours with reheating to 1100°C 30 minutes prior to, and subsequent to, each rolling pass. Final machining resulted in a 4 mm thick plate. A single bead-on-plate friction stir weld was performed by MegaStir Technologies [10,24] using a tool fabricated from an MS 80 grade of polycrystalline boron nitride featuring a convex scroll shoulder step spiral that did not require tilt. Plunge force was maintained at a constant 17.8 kN using a tool rotation speed of 500 rev·min^{-1} and a tool traverse rate of 25 mm·min^{-1}. These conditions correspond to the high heat input described in Refs. [6,10,12,22]. Although it is expected that there could be significant microstructure effects of the welding the thermomechanical affected zone (TMAZ) and heat affected zone (HAZ), to limit the scope of this study only the stir zone and base material will be considered. The material in the welded stir zone will be referred to as SZ hereafter, while that in the base material will be referred to as BM. The grain structure was previously analyzed using electron backscattered electron diffraction (EBSD) in Ref. [11]. The BM had an average grain diameter of 0.89 μm whereas the SZ had a starting grain material of 12.5 μm and the overall grain structure was found to be equiaxed [10,12].

Table 1: Composition of MA956 heat used in this research from [11] determined by inductively coupled plasma mass spectrometry and LECO analysis.

Alloy	Fe	Cr	Al	Y_2O_3	Ti	Mn	Si	Ni	C	Mo	S	P
MA956 (wt %)	Bal	19.93	4.75	0.51	0.39	0.09	0.08	0.04	0.023	0.02	0.008	0.006

2.1 Irradiation Conditions

Samples for irradiation were excised from the middle of the SZ and the BM using electrical discharge machining. Prior to irradiation, samples were mechanically polished to 1200 grit (P-4000) SiC paper followed by mechanical polishing to 1 μm diamond and a final polish using a vibratory polisher with a 0.02 μm silica solution.

Irradiations were performed at the Ion Beam Laboratory at Sandia National Laboratories, with a 6 MV Pelletron Tandem accelerator with 5 MeV Fe^{++} ions with a raster scanned beam. Dose was calculated at a depth of 600 nm beneath the irradiated surface using the Quick Kinchin Pease Mode in the Stopping

and Range of Ions in Matter (SRIM) with displacement damage of 40 eV [25]. The damage profile and implanted ion profile were presented in [22]. Dose rates varied between 0.44-2.3 x 10^{-4} dpa/s at the nominal depth of 600 nm. The effect of dose rate was not considered and an effort was made to maintain as consistent an irradiation dose as possible and stay within a factor of three. Samples were irradiated to 1 and 25 dpa at 400 and 500ºC. Temperatures were maintained and monitored using a LabVIEW controlled button heater and the temperature was kept within 2σ<5°C throughout the course of the irradiation. Pressures were maintained at ~10^{-5} Pa (~10^{-7}) torr throughout the irradiation. The data presented here will be combined with characterization results from [22] for a complete evaluation of irradiation temperature dependence.

2.2 Nanoindentation and Microindentation

Nanoindentation was conducted on each of the unirradiated specimens to assess the difference in hardness between material in the BM and that within the SZ. In addition, nanoindentation was conducted on a subset of irradiated specimens, including those irradiated to 1 and 25 dpa at 400°C and 500°C, to measure the effects of irradiation on mechanical properties.

The unirradiated specimens from both the BM and the SZ were each mounted in phenolic resin and subsequently mechanically polished through 1200 grit (P-4000) SiC paper, followed by mechanical polishing using 9, 3 and 1 μm diamond suspension, and finished by vibratory polishing with 0.05 μm alumina suspension. To enable analysis by EBSD, a final electropolishing procedure was performed at 20 V using an electrolyte containing 10% perchloric acid in ethanol maintained at 250 K (-23°C). These EBSD analyses were performed to study the grain structures prior to irradiation and were reported previously in [10,11]. The irradiated specimens, on the other hand, were adhered via mounting wax to a glass bed which was mounted to an aluminum puck. These specimens were also not electropolished. Given notable differences in mounting and required sample preparation prior to irradiation, the authors caution against directly comparing nanohardness results between the unirradiated and irradiated specimens.

Nanoindentation was conducted using a KLA-Tencor G200 nanoindenter with a Berkovich diamond tip indenter. Both the area function calibration and analysis were performed with the NanoSuite software provided by KLA. Tip area function calibration was performed with a sample of fused silica with known properties. A 2nd-order polynomial function was fitted to the projected area to depth relationship for the tip determined in the fused silica sample. Standard analysis of all data was performed using the Oliver-Pharr Method [26]. A surface detection threshold stiffness of 200 N m^{-1} was used to identify when the tip contacted the sample surface. Quasi-static loading and partial unloading was used to determine hardness and modulus. With quasi-static testing, the indenter head penetrates to a desired depth and holds, then measures the elastic stiffness upon retraction before being reinserted in the same location to measure hardness at progressively greater indentation depth. For this study, the target strain rate was 0.1 s^{-1} while the depth limit was set to 1000 nm with the number of cycles equal to 10. This approach yields only discrete depths at which properties are evaluated, but avoids any issues arising from the application of a harmonic stress to the material, such as with the continuous stiffness measurement (CSM) [27] and is consistent with recommendations in Ref. [28].

Nanoindentation of the irradiated specimens was applied parallel to the irradiating beam and into the irradiated surface. Each specimen was indented at 25 different locations, each laterally spaced at least 25-60 μm apart to avoid plastic zone interference between adjacent indents, as the plastic zone is expected have a radius ~4-10 times larger than the indentation depth [29–34]. The tip was loaded and unloaded at 10-20 depths per indent site. Each indentation load cycle included a 15-second load time and a 10-second hold at maximum load, followed by a 90% unload. From each indent location and each loading/unloading

point increment, an average depth and average hardness was calculated, along with the standard deviation and the standard deviation of the mean for both the depth and hardness values.

The average grain size in the SZ material (12.5 μm) is much larger than both the irradiation depth (~1.8 μm) and the likely plastic region of the indents from the nanoindentation, which are expected to be at least ~4 to 5 times [33] the indentation depth (~2.6 to 3.5 μm at depths of 650 nm). Due to this, indents in the SZ possibly only sampled single grains with some of the indents and did not always fully capture grain boundary strengthening. As a result, Vickers hardness measurements were conducted on each of the unirradiated specimens using a LECO LM100 Microhardness tester for comparison to the nanoindentation results and confirmation of the bulk sampling in the unirradiated materials. A total of 18 separate microhardness indents were conducted at a test force of 500 gf on each specimen and the standard deviation and standard deviation of the mean were determined.

2.3 Microstructure Characterization

Due to the shallow penetration depth of the Fe^{++} ions, it was necessary to prepare specimens for STEM and APT using liftout methods in a scanning electron microscope/focused ion beam (SEM/FIB) [35]. The SEM/FIBs employed were a ThermoFisher (formerly FEI) Nova 600 NanoLab DualBeam at Army Research Laboratory (ARL)-Aberdeen and the Naval Research Laboratory (NRL).

STEM lamellae were thinned to thicknesses below 200 nm with a 5 kV final polish. An attempt was made to analyze at least two liftouts per irradiation condition. STEM analysis was performed on JEOL 2100F or 2200FS TEM/STEM located at ARL and NRL, respectively, and a ThermoFisher (formerly FEI) Tecnai TF30-FEG STwin STEM analytic electron microscope located at CAES. Tilting of the sample was used to limit diffraction contrast such that all dispersoids were visible. Thickness was measured using electron energy loss spectroscopy zero loss method [36]. Regions of 500-700 nm below the irradiated surface was used for all analysis to bracket the calculated 25 dpa dose determined by SRIM [25] at a depth of 600 nm. The procedure for error analysis was the same as described in detail by Getto et al for irradiation-induced voids due to the similarity between voids and dispersoids in imaging [37]. Dislocation loops and networks were imaged using STEM bright field (BF) using a procedure described previously in [38] where on-zone or near zone STEM imaging excites all possible diffraction vectors for the zone axis, and also relaxes the g•b invisibility criterion allowing for faint contrast from in-plane [100](200) loops [38].

More detailed microstructural analysis was performed via APT, using a Cameca 4000X Si local electrode atom-probe with a 355 nm ultraviolet pulsed laser, a 40 K specimen base temperature, 60 pJ nominal laser pulse energy, a pulse repetition rate of 250 kHz, and a detection rate of 0.005 to 0.02 ions per pulse (0.5 to 2%). Specimens for APT were prepared using standard lift-out and milling procedures [39–42]. A subset of the irradiated specimens, 25 dpa at 400°C and 500°C, were analyzed, with particular emphasis on the evolution of the nanoscale oxides in the ODS material. For consistency, the same approach was applied to prior specimens, as received and irradiated at 450°C from [22] to enable a comprehensive understanding of nanocluster irradiation evolution dependencies on temperature and dose. In the irradiated material, liftouts were extracted 600 nm beneath the surface, providing a direct comparison with the 25 dpa irradiated material analyzed by STEM. Data reconstruction and analysis was performed using the Cameca Integrated Visualization and Analysis Software (IVAS) version 3.8.6. Data reconstruction was performed by calculating the tip radius from the specimen voltage, using default values of 1.65 for the image compression factor and 3.30 for the field factor, and assuming an evaporation field of 23 V mm^{-1} for Fe^{2+}. The reconstructions were also visually compared to SEM images of the APT specimens prior to analysis. Subsequent imaging was conducted using the AP Suite 6.1 software.

Several of the peaks within the mass-to-charge spectrum were identified as oxide-based molecular ions including AlO, YO, FeO, TiO, and CrO, which is typical for ODS alloys with oxide nanoparticles and dispersoids. Cluster analysis within each reconstruction was conducted using the maximum separation method [43] employed in IVAS. The success of this approach depends primarily on proper selection of d_{max} (the maximum distance of separation between two atoms in a cluster) and N_{min} (the minimum number of atoms required to identify a cluster). These parameters are selected independently for each sample reconstruction, as they can vary based upon the solute concentrations and distribution within the matrix, which can potentially vary depending on different irradiation conditions [44–47]. The approach here follows that prescribed by Kolli and Seidman [48] and refined by Williams et al. [49]. In practicality, the approach for selecting d_{max} is iterative and requires visual comparison between the images created via cluster analysis, images created using iso-concentration surfaces created with the Y, Ti, and O containing ions using a 4-6% concentration threshold and the reconstruction image with clustering solutes clearly visible. Incorrect selection of d_{max} will typically result in failure to identify clusters clearly visible in the reconstruction, splitting of individual clusters into multiple smaller clusters, or spurious identification of matrix clusters that are not visually detectable. Meanwhile, values for N_{min} are identified to minimize the number of random clusters detected. For this study, values for d_{max} ranged from 0.6 to 1.0 nm, while values for N_{min} ranged from 19 to 42 atoms for all samples. Each analysis was conducted with order of 1 and $d_{erosion}$ = 0.2 nm.

The IVAS cluster analysis provides an output CSV file containing radii, number density, and volume fraction of nanocluster in each sample. The Guinier diameter (D_G) is determined for each identified nanocluster [50,51], while number density (N_{nc}) is found by dividing the total number of nanoclusters identified in all samples of a given condition by the total analyzed volume from all tips of that specimen. Volume fraction of clusters (f_v) was subsequently determined by counting the total number of atoms within clusters and dividing by the total number of atoms in combined analysis volume for each specimen and irradiation condition. Finally, the output file from IVAS not only provides composition data for each of the nanoclusters, but also provides the composition of the surrounding matrix for each solute species, which is relevant for evaluating the effects of welding and irradiation on the migration of oxide-forming solutes.

3 Results

3.1 Nanoindentation and Microindentation Results

The nanoindentation hardness measurements are displayed in Figure 1 as a function of indentation depth beneath the surface for comparison between the unirradiated base metal and stir zone (Figure 1a); comparison of irradiations to 1 dpa at each temperature (Figure 1b); and comparison of irradiations to 25 dpa at 400°C and 500°C (Figure 1c). In each case, small indentation depths (< 300 nm) have abnormally small hardness values, likely due to indentation size effects and the imperfect surface finish resulting from the sample preparation process. Deeper indents in the irradiated specimens progressively sample more of the unirradiated substrate below each irradiated layer, which is approximated as a thin film of thickness ~1,800 nm. Prior studies have found that indents conducted at <1/3 of the irradiated layer thickness are considered to be most representative of the hardness of the irradiated layer [52]. This compromise is based on avoiding the indentation size effects at shallower indents and avoiding excessive oversampling of the unirradiated substrate. As a result, a region at indentation depths between 475 nm and 675 nm is used as indicated in Figure 1, for which the hardness values were used to calculate an average hardness and the standard deviation of the mean to determine an estimated mean hardness for each specimen (Figure 1d). In reality, the change in hardness between the specimens irradiated at different temperatures remains reasonably consistent throughout the indentation depths above ~300 nm, so the comparison region primarily

provides an objective baseline depth for consistent comparison across the samples. For the unirradiated specimens, there is no concern about oversampling the substrate, so the hardness is approximated at the deepest indentation depth. It is acknowledged that deeper indentation would likely yield a more accurate bulk hardness. As a result, Vickers hardness measurements of the unirradiated specimens are conducted to provide an alternate comparison.

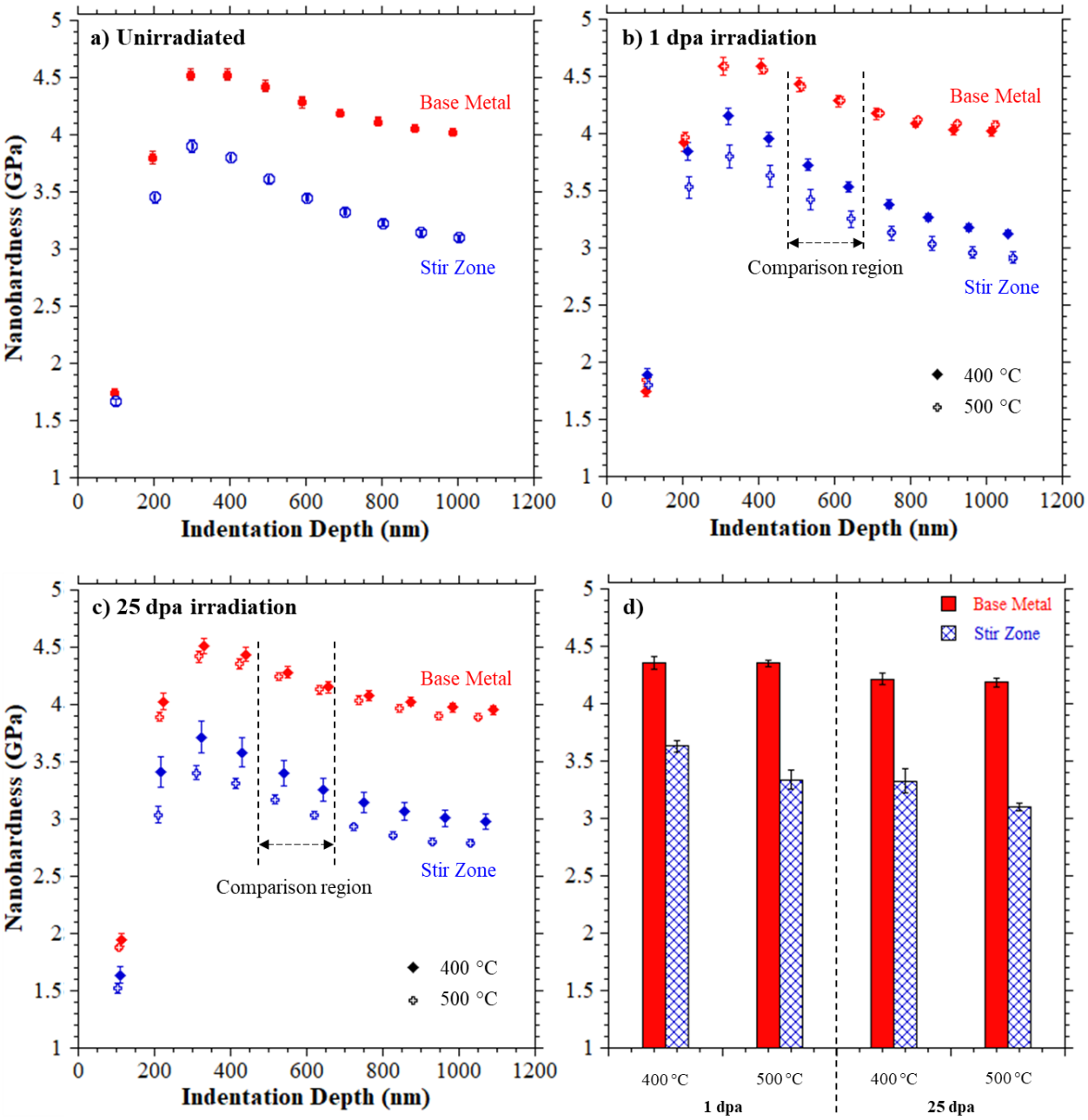

Figure 1: Summary of nanoindentation results in MA956 within the base metal and the friction stir welded stir zone (SZ) for the a) unirradiated (UI), b) 5 MeV Fe^{2+} ion irradiated to 1 dpa, and c) 5 MeV Fe^{2+} ion irradiated to 25 dpa. Image d) illustrates a comparison of the average hardness in the range of 475 to 675 nm. Error bars represent the standard deviation of the mean.

The BM nanohardness is 4.02 ± 0.03 GPa at indentation depths of ~1μm, corresponding well with other ferritic ODS alloys including model Fe-9%Cr ODS [33], Fe-9%Cr ODS alloys [53,54], and several other ODS alloys [55]. In the SZ, the nanohardness at comparable indentation depths decreases significantly to 3.53 ± 0.04 GPa, which is consistent with previous studies indicating significant softening of ODS alloys after FSW [11,56,57]. Following each irradiation, the SZ is observed to be consistently softer by 0.7 to 1.1 GPa (Figure 1), regardless of the irradiation dose and temperature, suggesting that the microstructure changes resulting in softening due to FSW are superimposed upon any irradiation effects on the respective microstructures. Upon further inspection of Figure 1d, it was also observed that each irradiation to 25 dpa results in slightly lower hardness (~0.14 to 0.17 GPa) than the 1 dpa irradiations at both 400°C and 500°C, respectively. Finally, the hardness of the BM does not appear to have any tangible dependence on the irradiation temperature for either dose level, while the SZ hardness is observed to decrease with increasing irradiation temperature (~0.25 to 0.29 GPa) between 400°C and 500°C. These irradiation-induced changes in hardness imply that irradiation-induced effects on microstructure also influence the strengthening mechanisms in both the BM and SZ. As a general rule, recrystallization for most metals is expected in the 0.33-0.5T_m region, which might impact the 500°C condition. Studies of similar ferritic alloys including T91 [58] and ferritic Fe-18Mn-0.6C-1.5Al TWIP steel [59] indicate no recrystallization, partial or otherwise, until 600°C so although this is possible it is not likely in the experimental conditions examined here.

The Vickers hardness of unirradiated MA956 BM averaged 365 ± 1.4 kgf/mm^2. In the SZ following friction stir welding, the Vickers hardness is 265 ± 2.7 kgf/mm^2, representing a reduction in microhardness of ΔH_v = 100 kgf/mm^2. These measurements, along with the nanohardness results are particularly helpful in estimating changes in yield strength as a result of friction stir welding. The empirical relationship from [60] was used:

$$\Delta\sigma_y = 3.06\Delta H_v \quad (1)$$

with $\Delta\sigma_y$ representing the increase in yield strength (in MPa) due to irradiation and ΔH_v as the measured increase in Vickers hardness (in kgf/mm^2). Applying Eq. 1 for the microhardness measurements estimates an ~300 MPa reduction in yield strength due to friction stir welding. Using the nanoindentation measurements, the relationship developed by Fischer-Cripps was used to convert Meyer hardness (in GPa as measured by nanoindentation) into Vickers hardness (in kgf/mm^2) via $H_V = 94.495H_{Meyer}$ [61]. Following this approach, the decrease in yield strength in the SZ is estimated to be within the range from 211 to 314 MPa, which is reasonably consistent with the microindentation results. Meanwhile, increasing the radiation dose from 1 to 25 dpa in each specimen appears to result in a 42 to 88 MPa reduction in yield strength and increasing irradiation temperature from 400°C to 500°C results in a 2 to 85 MPa reduction in yield strength. A summary of the measured nanohardness and changes in hardness and yield strength between the BM and SZ for each specimen is provided in Table 2.

Table 2: Measured nanohardness values for each specimen within the comparison region indentation depths, along with estimated changes in hardness and yield strength within the stir zone.

MA956 specimen	BM Nanohardness, H_{Berk} (GPa)	SZ Nanohardness, H_{Berk} (GPa)	BM – SZ ΔH_{Berk} (GPa)	BM – SZ $\Delta\sigma_y$ (MPa)
1 dpa, 400°C	4.36 ± 0.05	3.63 ± 0.05	-0.73	-211
1 dpa, 500°C	4.35 ± 0.03	3.34 ± 0.08	-1.01	-293
25 dpa, 400°C	4.21 ± 0.05	3.33 ± 0.11	-0.89	-257
25 dpa, 500°C	4.19 ± 0.04	3.10 ± 0.03	-1.08	-314

3.2 Microstructure Analysis

To explain the nanoindentation results, a careful assessment of the microstructure including nanoclustering, dispersoids and dislocations was performed by STEM and APT characterization.

3.2.1 Dispersoid Evolution

Figure 2 shows HAADF micrographs of the BM after self-ion irradiation to 1 and 25 dpa. The light grey layer on the top of all HAADF images is the Pt layer retained from the FIB liftout process. Note that Y-Al-O or Y-O precipitates show as dark circles because the mechanism of contrast in STEM HAADF imaging is Z contrast such that low Z features show up as darker than the surrounding matrix. A thin oxide (black) formed at the surface under some irradiation conditions. The white areas in Figure 2c are a result of diffraction contrast in individual grains; to verify all dispersoids were observed, the sample was tilted to multiple angles so all grains could be clearly imaged. Through the tilting process, grains with high contrast would become clearer verifying that the white areas or contrast were not dispersoids or loops. Figure 3 includes a magnified image of the dispersoids at 400ºC, 25 dpa. Dispersoids were more or less randomly distributed even after irradiation. There were no indicators of ballistic dissolution such as “haloing” of smaller precipitates around a larger dispersoid, as observed by Chen et al in [8]. Figure 4 shows HAADF micrographs of the self-ion irradiated MA956 SZ at 1 and 25 dpa. There appeared to be formation of new dispersoids relative at 25 dpa relative to 1 dpa. However, when compared to the BM in Figure 2, there are fewer dispersoids in all SZ irradiated conditions.

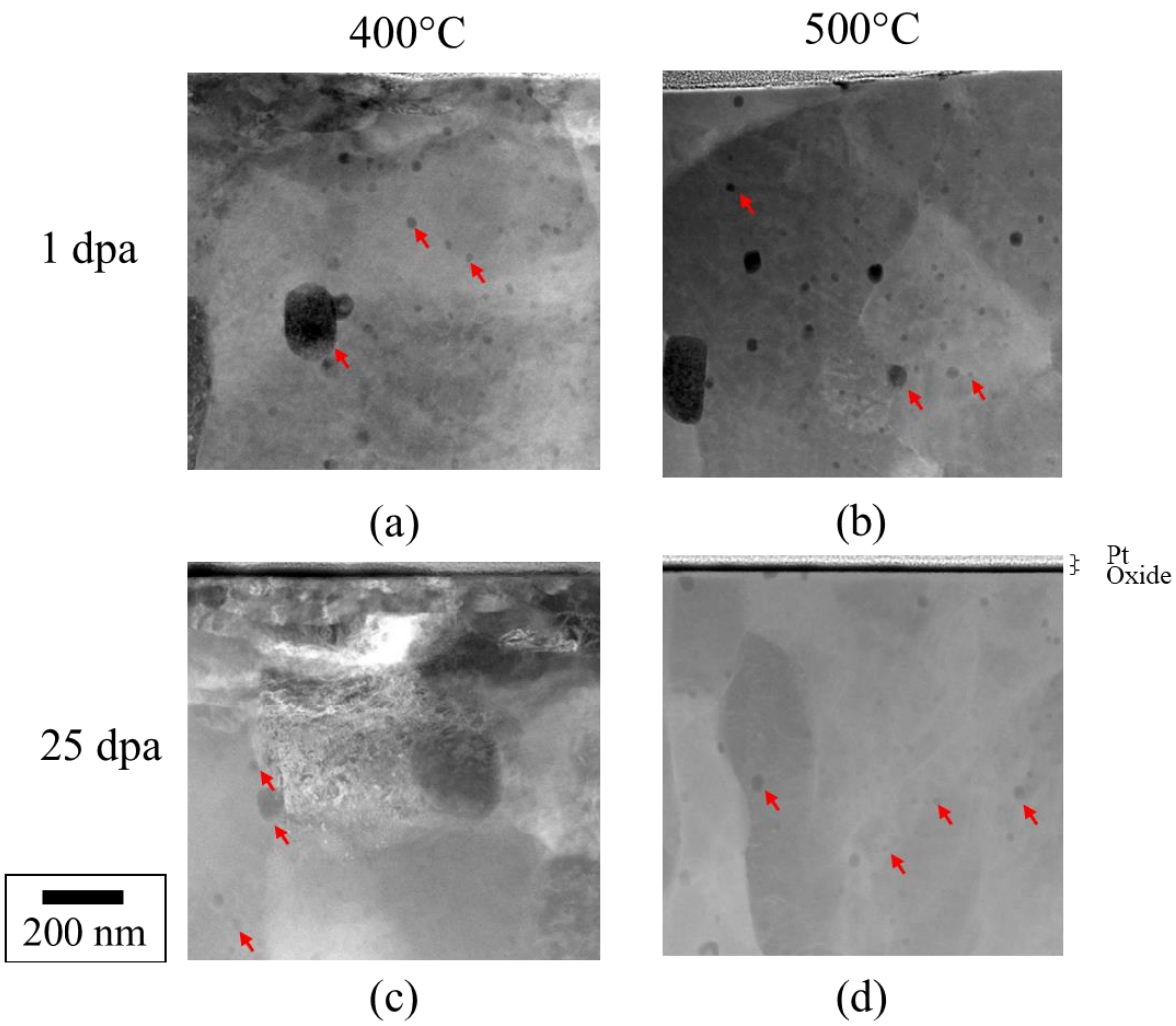

Figure 2: HAADF images of MA956 base material irradiated at 1 dpa at a) 400°C and b) 500°C and to 25 dpa at c) 400°C and d) 500°C. Select dispersoids marked with red arrows.

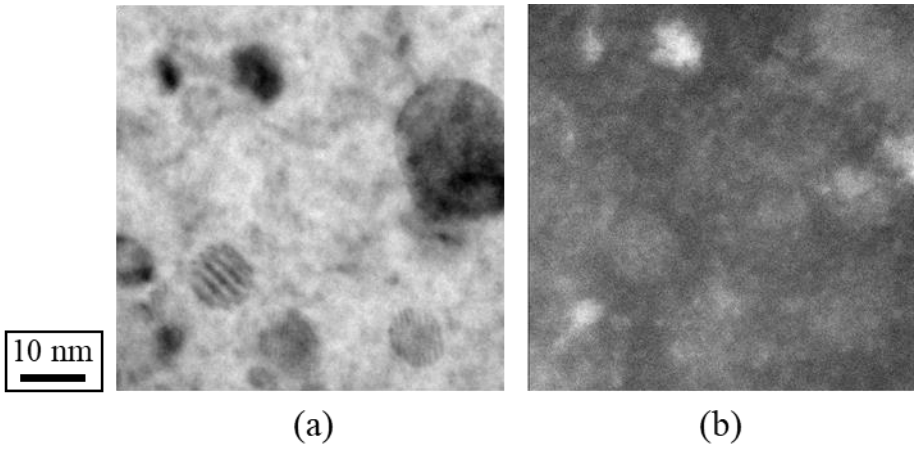

Figure 3: a) Bright field and b) high angular annular dark field images of dispersoids observed in the base mater at 440C, 25 dpa.

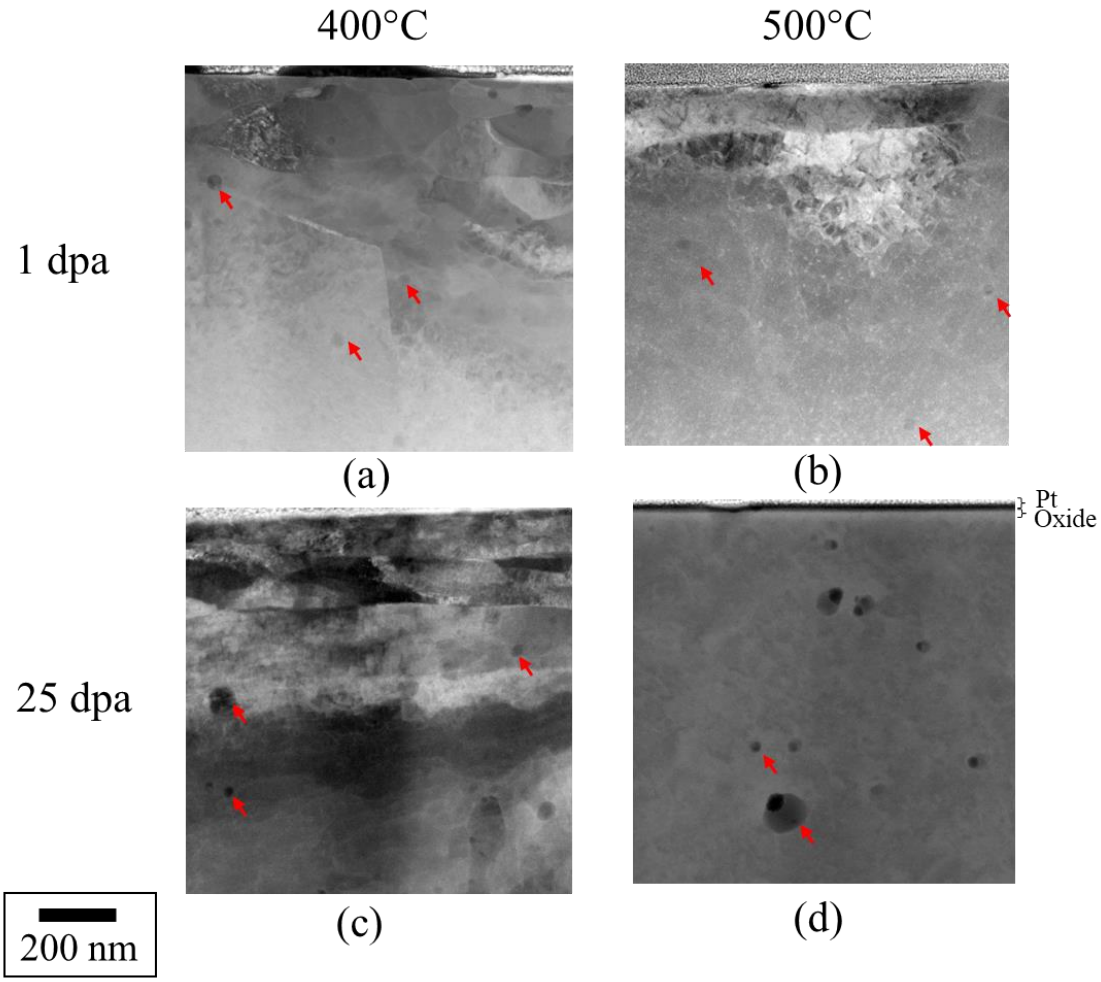

Figure 4: HAADF images of MA956 stir zone irradiated at 1 dpa at a) 400°C b) 500°C and to 25 dpa at c) 400°C d) 500°C. Select dispersoids marked with red arrows.

Dispersoids were quantified according the procedure described in Section 2.3. Due to the peaked irradiation profile, it is most appropriate to consider only dispersoids found 500 to 700 nm from the irradiated surface, which brackets the nominal, calculated 25 dpa dose at 600 nm and is consistent with the depth range selected for nanoindentation measurements in Figure 1. Data for the unirradiated BM, 450ºC, 1 and 25 dpa are repeated from [22] to provide a more complete temperature dataset. An additional liftout to improve statistics for the unirradiated SZ was included in this study. The diameter of the dispersoids observed in the BM, before and after irradiation, is displayed in Figure 5a (solid red). Within the BM, the dispersoid diameter tends to increase with increasing irradiation dose and temperature. Two additional observations are worth noting; first, there was a small decrease in diameter at 400°C from 0 (10.6±1.0 nm) to 1 dpa (8.1±1.0 nm) followed by an increase to 25 dpa (10.8±1.0 nm). This was attributed to the formation of new, smaller dispersoids with irradiation. Second, 500°C exhibited the most growth from 0 dpa to 25 dpa. Likewise, the diameter of the SZ is plotted (hatched blue) in Figure 5a. The diameter of the SZ dispersoids remains higher than the BM regardless of temperature or dose. At 400ºC, the diameter remained nearly within error bars from 19.7±1.0 nm to 18.0±1.0 nm from 0 to 25 dpa. At 400 and 450°C, the diameter increased from 0 to 25 dpa. Regardless, the trend of increased growth with dose and temperature was observed.

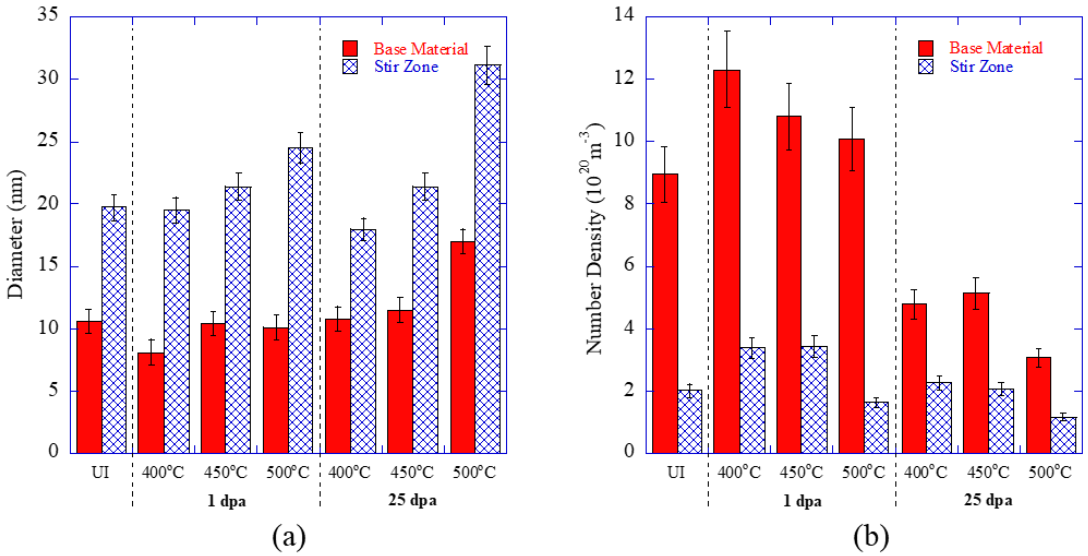

Figure 5: Evolution of dispersoid a) diameter and b) number density for the base material and stir zone in MA956 irradiated with 5 MeV Fe^{++} up to 25 dpa at 400°C, 450°C [22] and 500°C. All data was taken in the 500 to 700 nm depth region.

Number density for the BM is plotted in Figure 5b (solid red). An initial increase in number density was observed at all temperatures from 0 to 1 dpa. The increase was the largest at 400ºC from $8.96\pm0.9\times10^{20}$ m^{-3} to $12.3\pm1.2\times10^{20}$ m^{-3}. After the initial increase to 1 dpa, there was a decrease in number density by 25 dpa to $4.79\pm0.5\times10^{20}$ m^{-3}. This is likely indicating initial precipitation of new phases followed by Ostwald coarsening, which has been observed at higher doses in this material [6] and other alloys [62,63]. The number density of the stir zone is plotted in Figure 5b (hatched blue) and followed similar trends with dose, but was lower than the base material across all irradiation conditions. By 25 dpa, the number density is much more similar between the BM and the SZ; at 500°C: 25 dpa the number density for base material and stir zone is $3.06\pm0.3\times10^{20}$ m^{-3} and $1.17\pm0.1\times10^{20}$ m^{-3}, respectively. The decrease in number density from 1 to 25 dpa in BM was stronger than that observed in the SZ. A summary of all dispersoid results along with dislocation results is presented in Table 3.

Table 3: Summary of microstructure data for 5 MeV Fe^{2+} ion-irradiated MA956 base material and friction stir welded stir zone. Data at 450ºC repeated from [22] to provide a more complete data set. All dispersoid and dislocation data were obtained via STEM imaging.

Experimental Conditions			Dispersoids				Dislocations					
Temperature (°C)	Dose (dpa)	Sample Status	Number of Precipitates	Precipitate diameter (nm)	Precipitate Density (10^{20} m^{-3})	Sink Strength (10^{14} m^{-2})	Number of Loops	Loop Diameter (nm)	Loop Number Density (10^{20} m^{-3})	Loop Line Length (10^{14} m^{-2})	Network Line Length (10^{14} m^{-2})	Total Loop + Line Length (10^{14} m^{-2})
As received	N/A	BM [22]	263	10.6±1.0	8.96±0.9	1.19±0.1	N/A	N/A	N/A	N/A	0.614±0.1	0.614±0.1
		SZ	103	19.7±1.0	2.01±0.2	0.50±0.05	N/A	N/A	N/A	N/A	0.675±0.1	0.675±0.1
400	1	BM	536	8.1±1.0	12.3±1.2	1.25±0.1	70	9.5±1.0	35.2±7.0	2.1±0.5	1.6±0.4	3.7±0.9
		SZ	275	19.5±1.0	3.37±0.4	0.83±0.08	70	12.6±1.0	18.0±4.0	1.4±0.3	1.0±0.2	2.5±0.7
	25	BM	446	10.8±1.0	4.79±0.5	0.65±0.07	14	28.0±1.0	6.0±1.2	1.0±0.2	1.1±0.2	2.1±0.5
		SZ	67	18.0±1.0	2.25±0.2	0.51±0.05	44	15.8±1.0	13.0±2.6	1.3±0.2	1.1±0.2	2.4±0.7
450	1	BM [22]	393	10.4±1.0	10.8±1.0	1.41±0.1	17	20.2±1.0	6.2±1.2	0.8±0.2	1.2±0.3	2.0±0.5
		SZ [22]	68	21.4±1.0	3.43±0.3	0.92±0.09	32	19.7±1.0	5.8±1.2	0.7±0.1	1.4±0.4	2.1±0.5
	25	BM [22]	164	11.5±1.0	5.13±0.5	0.74±0.07	40	20.6±1.0	6.3±1.2	0.8±0.2	0.7±0.2	1.5±0.4
		SZ [22]	149	21.4±1.0	2.06±0.2	0.55±0.06	35	15.6±1.0	10.3±2.0	1.0±0.2	0.6±0.2	1.6±0.4
500	1	BM	662	10.1±1.0	10.1±1.0	1.28±0.1	21	20.9±1.0	1.9±0.4	0.3±0.1	0.9±0.2	1.2±0.3
		SZ	103	24.5±1.0	1.64±0.2	0.51±0.05	21	22.1±1.0	2.7±0.6	0.4±0.1	0.9±0.2	1.3±0.3
	25	BM	271	17.0±1.0	3.06±0.3	0.65±0.07	19	37.0±1.0	4.9±1.0	1.2±0.3	1.4±0.4	2.5±0.7
		SZ	104	31.1±1.0	1.17±0.1	0.46±0.05	20	50.6 ±1.0	0.9±0.2	1.1±0.2	0.6±0.2	1.7±0.5

3.2.2 Dislocation Evolution

A selection of representative BF images showing dislocation loops are shown in Figure 6. In a previous work [22], identified loops were confirmed to be **a**<100> or **a/2**<111> using conventional transmission electron microscopy with selected area electron diffraction, which is consistent with other ferritic alloys [64–66]. Since all loops were of the type **a**<100> and **a/2**<111>, Parish's method for on zone axis STEM imaging [38] for loop counting and size determination was used. Large dislocation loops (greater than 10 nm) formed by 1 dpa in both the BM and SZ material. Figure 7 shows the quantified data, which is also summarized in Table 3. The diameters of dislocation loops in the BM (solid red) and SZ (hatched blue) is shown in Figure 7a. With increasing dose as well as irradiation temperature, the dislocation loop diameter tends to increase, consistent with other ferritic or ferritic-martensitic alloys [3,65,66]. There was no systematic trend with dislocation loop diameter being larger for either the BM or SZ. About half of experimental conditions are within experimental error and after 25 dpa irradiation, the BM contained larger loops than at 400°C and 450°C but not at 500°C. Figure 7b shows the loop number density, which was inversely proportional to irradiation temperature, similar to trends in the dispersoid number density (Figure 5b). The number density of loops within the SZ tended to be higher or within experimental error than BM for a given irradiation condition, with the outlier of 400°C, 1 dpa where BM had an extremely high loop number density of $35.2\pm7.0\times10^{20}$ m^{-3}. With dose, at 450 and 500°C, the number density remains nearly constant whereas at 400°C there was a decrease from 1 to 25 dpa for both the base material ($35.2\pm7.0\times10^{20}$ m^{-3} to $6.0\pm1.2\times10^{20}$ m^{-3}) and the stir zone ($18.0\pm4.0\times10^{20}$ m^{-3} to $13.0\pm2.6\times10^{20}$ m^{-3}). Figure 7c shows the change in network line density. An initial increase from 0 to 1 dpa was observed followed by a plateau or slight decrease from 1 to 25 dpa for both BM and the SZ. The network line density was very similar between BM and SZ at a given irradiation condition

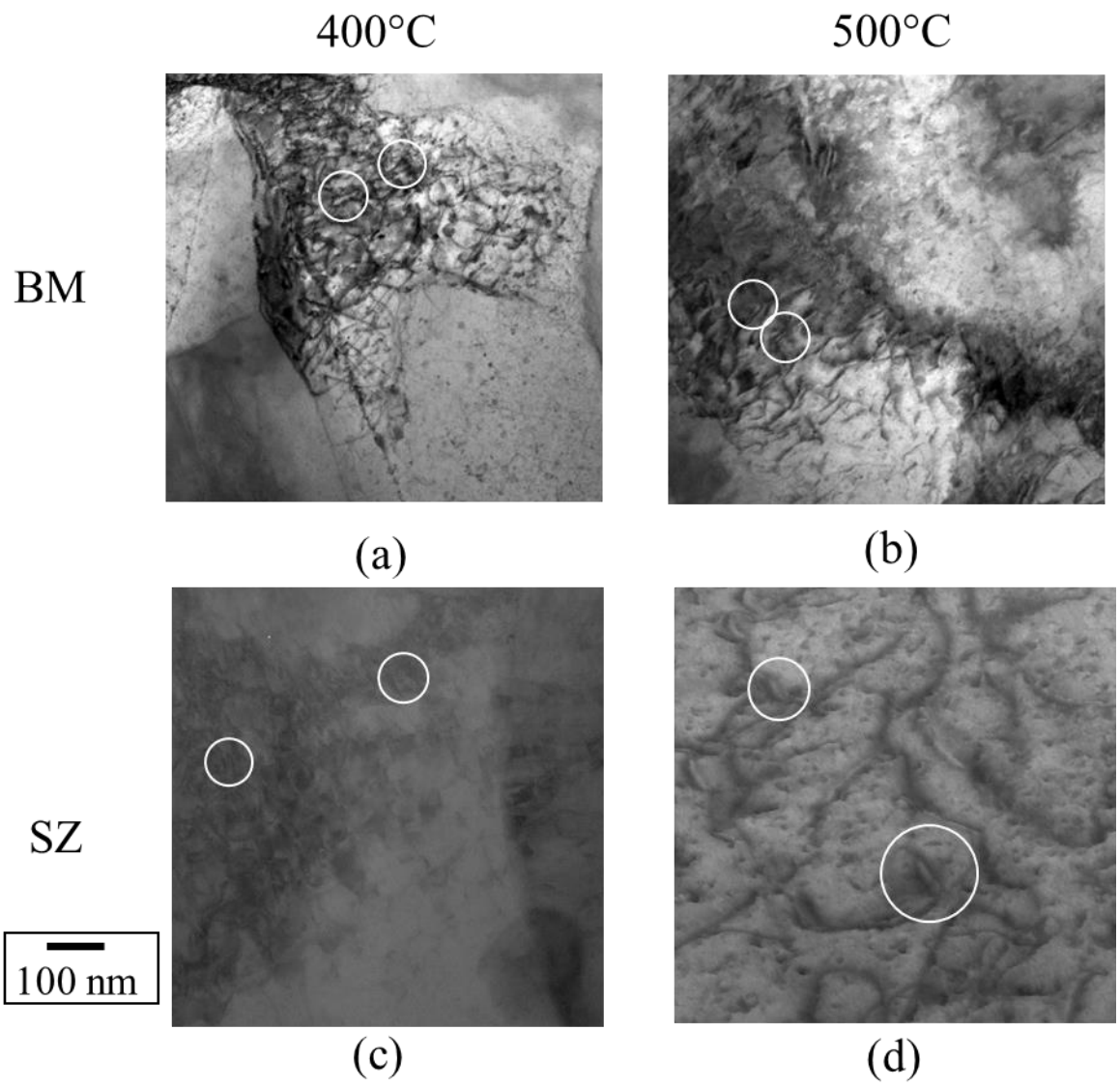

Figure 6: STEM BF images of dislocation loops and network in MA956 at 25 dpa for the BM at a) 400 and b) 500°C and the SZ at c) 400 and d) 500°C. White circles highlight selected loops.

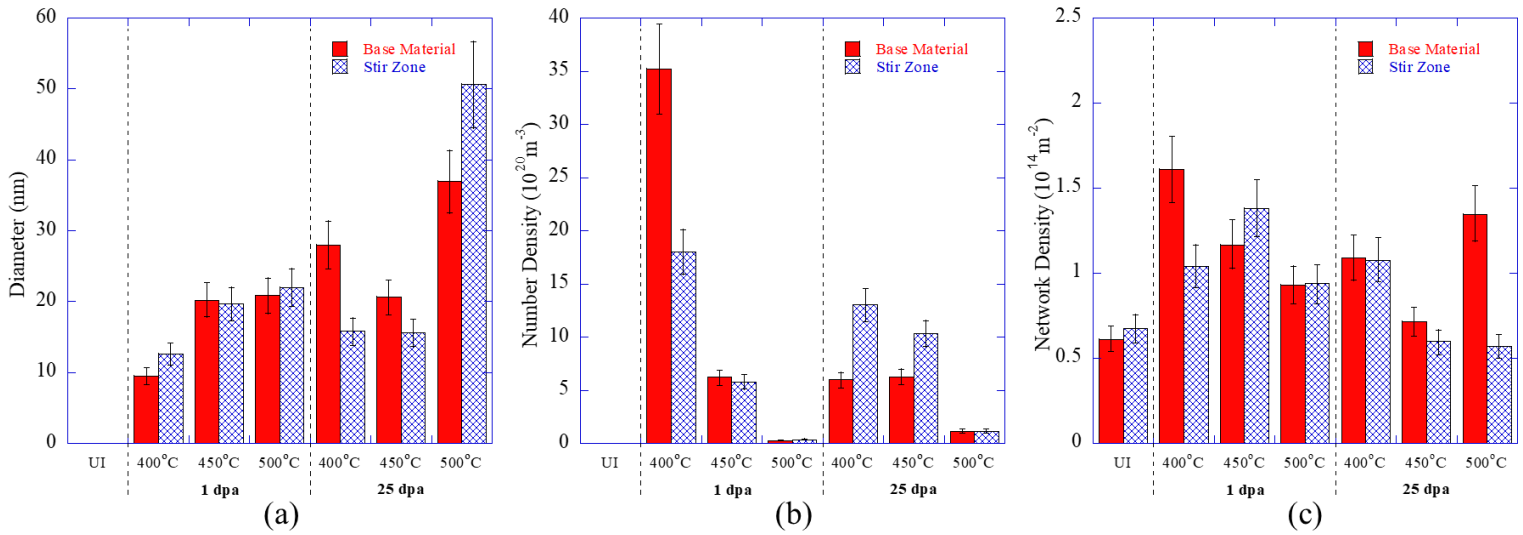

Figure 7: Evolution of dislocation loop a) diameter, b) number density, and c) network line length in base material (solid red) and stir zone (hatched blue) in MA956 irradiated at 400, 450 [22] and 500°C up to 25 dpa.

3.2.3 Atom Probe Tomography

APT reconstructions from the BM are displayed in Figure 8 for the unirradiated specimen and the samples irradiated to 25 dpa at temperatures ranging from 400 to 500°C. Each of these datasets exhibit strong evidence of clustering of Y, O, Ti solutes as well as YO, TiO, FeO, CrO, and AlO molecular ions at common locations in the matrix, comprising the oxide nanoclusters. As a result, each of these ions and molecular ions are chosen for the cluster analysis. Figure 8 also illustrates the identification of oxide nanoclusters using isoconcentration surfaces and via the cluster analysis. These images, along with the solute distributions, are compared to ensure a visual match between the observed oxides and the two algorithm identified nanoclusters. Interestingly, single ion solutes of Fe, Cr, and Al did not exhibit nanoclustering when viewed in isolation.

The average D_G for each nanocluster was determined using the output file from the IVAS software, and particle size distributions for each specimen are provided in Figure 9. In several instances, a mix of smaller and larger oxide clusters are present; a good example of this is the 400°C, 25 dpa dataset which contains several large clusters up to ~40 nm in diameter. These larger clusters are likely the same type as those identified as dispersoids by STEM analysis. To avoid double identification of larger dispersoids via STEM and clusters via APT, any nanoclusters with D_G larger than 14.5 nm are classified as "dispersoids." This threshold was identified by inspection of each particle size distribution and approximating the end of the tail for the smaller cluster distribution. This effectively removes a small number of larger clusters and minimizes any double counting of larger STEM-visible dispersoids and APT-identified nanoclusters. Using this smaller distribution for nanoclusters in each specimen, a summary of the oxide nanocluster average sizes and number densities are provided in Table 4. There is some overlap between the STEM-identified dispersoids (below 14.5 nm) and the APT-identified nanoclusters, but the APT-identified clusters in this size range are more numerous by ~2-3 orders of magnitude, so any double-counting is minimal. APT-identified nanoclusters are found to have an average D_G of 7.42 ± 0.10 nm before irradiation. Following irradiation to 25 dpa, nanoclusters have finer morphology with diameters of 5.44 ± 0.16 nm, 5.57 ± 0.15 nm, and 6.94 ± 0.07 nm for irradiations temperatures of 400°C, 450°C, and 500°C, respectively, with larger clusters corresponding to higher irradiation temperatures. Number densities following each irradiation are reasonably consistent ranging from 100 to 114 × 10^{21} m^{-3}, but the number density in the unirradiated specimen is lower (40 × 10^{21} m^{-3}). However, the unirradiated specimen also contained the largest analysis volume, including one large LEAP dataset with 648 million ions. Throughout this sample, the distribution of oxide nanoclusters is not homogeneous and includes several denuded regions, causing the number density to appear lower than the other specimens which did not generate comparably large datasets. Alternatively, the formation of new nanoclusters upon irradiation is consistent with the increase in number density of the STEM-identified dispersoids here and in [6,22].

α' was not observed in this alloy at any of the irradiated conditions in APT or STEM analysis. A recent study by from Reese et al [68] demonstrating that there is no alpha prime Fe-18Cr observed above 10^{-4} dpa/s, which is around our dose rates and likely depends on the same balancing of radiation enhanced diffusion versus ballistic dissolution similar to the dispersoid kinetics discussed here and at higher doses in MA956 both welded and base material [6,23]. In another study [69], Ke et al. utilized a phase field approach in Fe-Cr alloys suggesting that α' is unlikely to occur at dose rates above ~10^{-5} dpa/s.

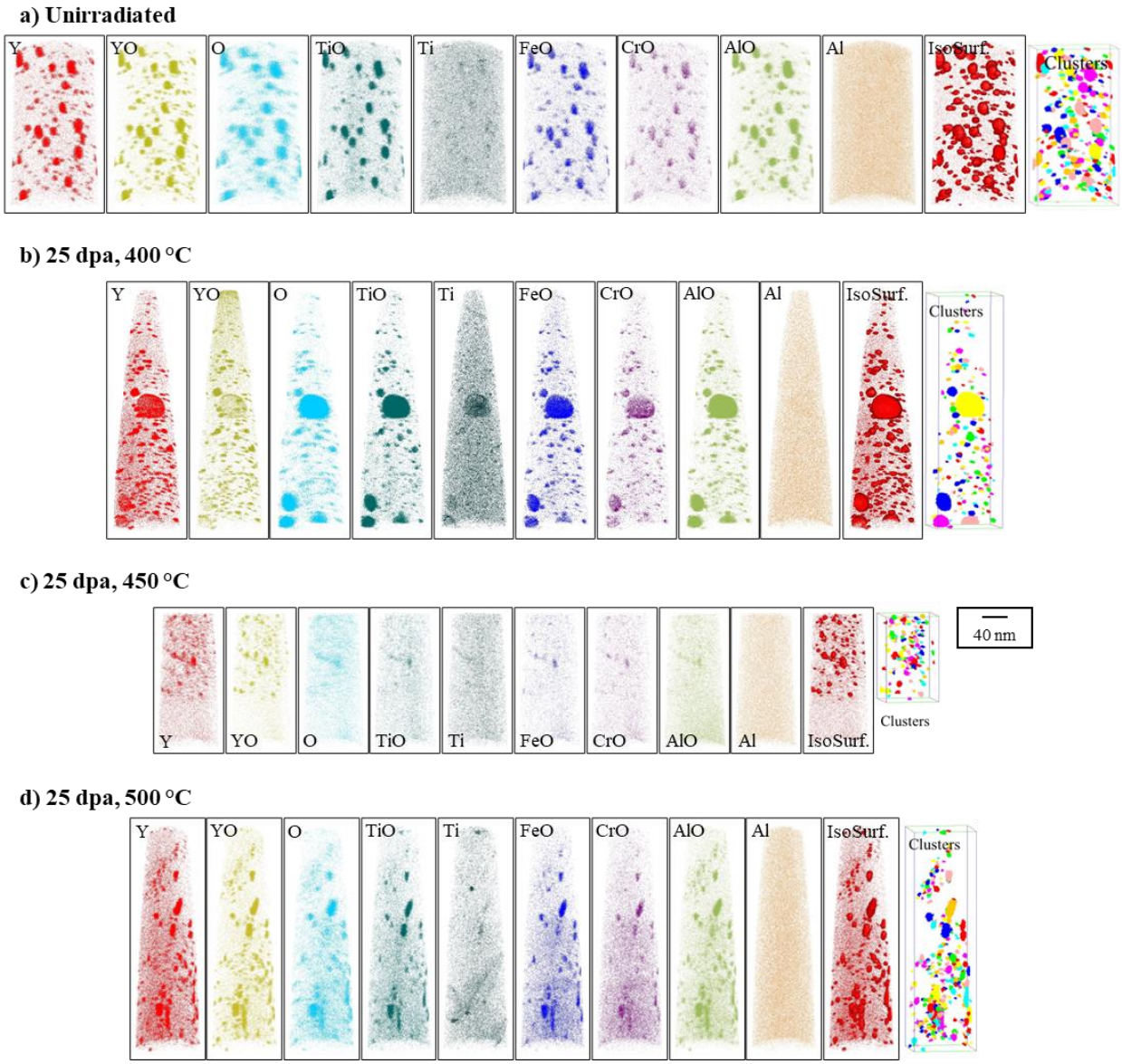

Figure 8: 3D atom distribution maps for oxide nanocluster solutes in MA956 BM for a) unirradiated, and following 5 MeV Fe^{2+} irradiation to 25 dpa at b) 400°C, c) 450°C, and d) 500°C, respectively. The raw data (RHIT files) for a) and c) from [22] were reanalyzed here for a complete cluster and matrix composition analysis.

Table 4: Summary of oxide nanocluster morphology and chemistry, and surrounding matrix chemistry for MA956 BM via APT. Reported errors are the standard deviation of the mean.

Feature	Unirradiated	Fe^{2+} irradiated (25 dpa, 400°C)	Fe^{2+} irradiated (25 dpa, 450°C)	Fe^{2+} irradiated (25 dpa, 500°C)
Analysis volume (nm^3)	12,025,175	1,617,300	1,102,445	5,217,925
Oxide Nanoclusters				
# of nanoclusters measured	473	165	119	616
Average diameter, D_G (nm)	7.42 ± 0.10	5.44 ± 0.16	5.57 ± 0.15	6.94 ± 0.07
Number density, N_{nc} ($\times 10^{21}$ m^{-3})	40	100	108	114
Volume fraction, f_v	0.93%	1.26%	0.64%	1.50%
Sink strength (10^{14} m^{-2})	37.3	68.4	75.6	99.4
Y:Ti	5.53 ± 0.13	3.59 ± 0.13	7.07 ± 0.62	7.97 ± 0.20
(Y+Ti):O	1.24 ± 0.01	1.09 ± 0.02	1.28 ± 0.02	1.21 ± 0.01
Al:O	3.14 ± 0.04	2.09 ± 0.04	2.56 ± 0.06	3.68 ± 0.04
Matrix Composition (at%)				
Cr	19.4	19.6	17.7	19.4
Al	8.7	8.2	8.3	8.3
Y	0.05	0.12	0.08	0.09
Ti	0.07	0.12	0.08	0.07
O	0.13	0.26	0.26	0.22
Y+Ti+O	0.25	0.50	0.42	0.37

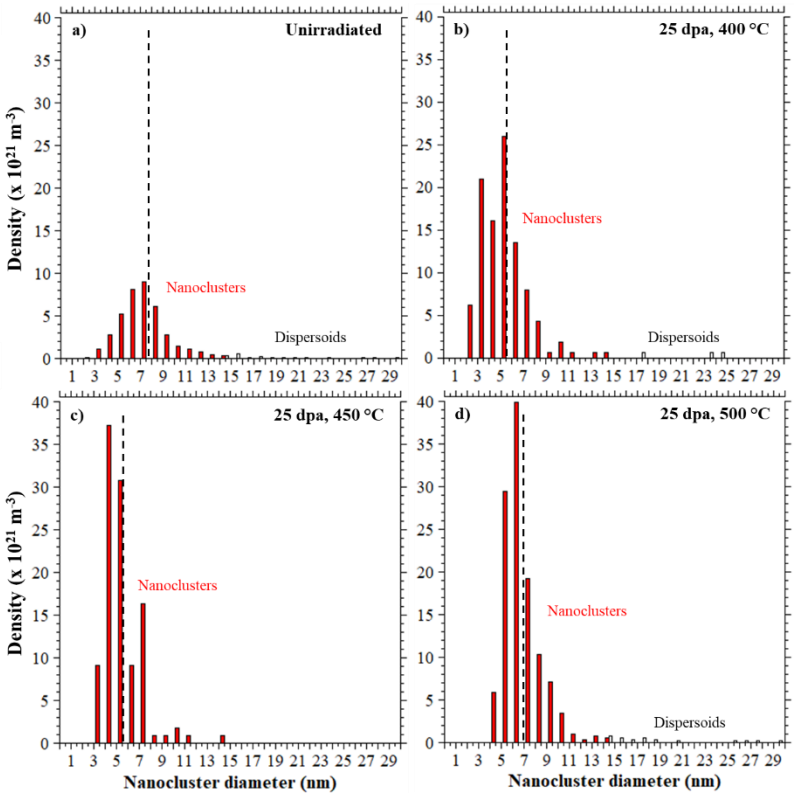

Figure 9: Nanocluster particle size distributions for MA956 base metal (BM) with relative density for a) unirradiated, following 5 MeV Fe^{2+} irradiation to 25 dpa at b) 400°C, c) 450°C, and d) 500°C, respectively. Dashed lines represent the average size for each specimen.

Table 4 also provides chemical information for both the nanoclusters and the surrounding matrix in the BM. Since the solutes Y, Ti, O, and Al are so closely affiliated with the oxides, it is often helpful to compare solute ratios with the clusters to gain insights into the effects of irradiation. The Y:Ti ratio starts at 5.53 ± 0.13 in the unirradiated condition, but is reduced to 3.59 ± 0.13 at the lower irradiation temperature (400°C), yet is progressively increased at the higher irradiation temperatures. A similar trend is observed for the Al:O value, which reduces from 3.14 ± 0.04 to 2.09 ± 0.04 at 400°C irradiation to 25 dpa, but is again slightly higher at 500°C (3.68 ± 0.04). The (Y+Ti):O value is also slightly reduced at 400°C, but is stable at the higher temperatures with values ranging from 1.21 to 1.28, and is consistent with (Y+Ti):O values in a model Fe-9%Cr ODS reported by Swenson and Wharry [47], which ranged from 1.16 to 1.26. These patterns confirm that dissolution of the nanoclusters is more favorable at the lower irradiation temperature, consistent with smaller cluster sizes resulting at 400°C and 450°C, respectively. Conversely, a corresponding increase in the matrix composition for Y, Ti, and O due to partial dissolution of the clusters was observed, with the 400°C irradiation leading to the most dramatic increase in solid solution. The reduced size of the nanoclusters following each irradiation are expected to influence the strengthening from dispersed barriers, while the increase in matrix composition likely impacts solid solution strengthening of the irradiated alloy as well.

APT reconstructions of the SZ are displayed in Figure 10 for the unirradiated specimen and the samples irradiated to 25 dpa at temperatures ranging from 400 to 500°C. None of these datasets exhibit substantial clustering of Y, O, Ti solutes or YO, TiO, FeO, CrO, and AlO molecular ions. This result indicates that friction stir welding has resulted in removal of the oxide nanoclusters, while irradiation to 25 dpa has not resulted in any substantial nucleation of new nanoclusters within the matrix. In a few instances, some evidence of Ti segregation to dislocation lines is present and visible in Figure 10 following irradiation to 25 dpa at each temperature. Furthermore, three or four oxide Y-Ti-O-rich clusters were found in the 450°C, 25 dpa specimen (shown in Figure 10), but this is not nearly as significant of a morphology as in the BM specimens. Even though nanoclusters are not present in the SZ specimens, IVAS still enables measurement of the matrix compositions (provided in Table 5). For each solute (Y, Ti, and O), matrix compositions are lower in the SZ than in the BM specimens, suggesting that friction stir welding has resulted in higher amounts of precipitation or segregation away from the matrix (i.e. on grain boundaries or carbides). Interestingly, the matrix composition of these solutes is highest following 450°C irradiation, particularly for Ti. The explanation for this is not clear.

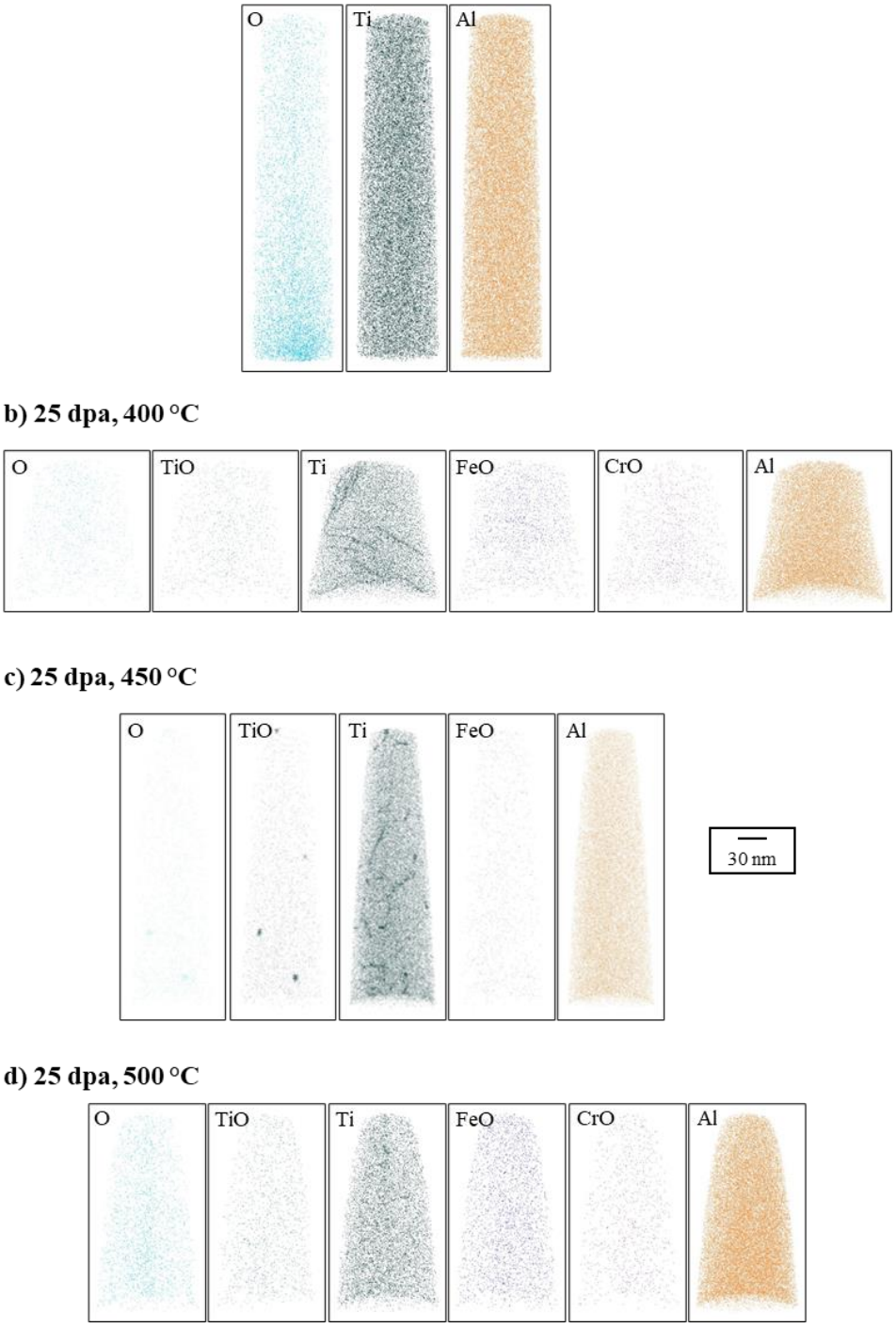

Figure 10: 3D atom distribution maps for oxide solutes in MA956 stir zone (SZ) for a) unirradiated, and following 5 MeV Fe^{2+} irradiation to 25 dpa at b) 400°C, c) 450°C, and d) 500°C, respectively. The raw data (RHIT files) for a) and c) were from [22] were reanalyzed here for a complete cluster and matrix composition analysis. Images shown are only for ions exhibiting resolvable peaks in each mass-to-charge spectrum, respectively.

Table 5: Summary of matrix chemistry for MA956 stir zone (SZ) via APT.

Feature	Unirradiated	Fe^{2+} irradiated (25 dpa, 400°C)	Fe^{2+} irradiated (25 dpa, 450°C)	Fe^{2+} irradiated (25 dpa, 500°C)
Analysis volume (nm^3)	1,530,107	1,800,578	3,781,196	1,200,447
Matrix Composition (at%)				
Cr	19.5	19.1	18.2	19.5
Al	8.6	8.2	8.1	8.5
Y	<0.005	<0.005	<0.005	<0.005
Ti	0.05	0.04	0.10	0.03
O	0.07	0.09	0.11	0.09
Y+Ti+O	0.12	0.12	0.21	0.11

Inconsistencies between results from STEM and APT were noted. First, in the BM samples, the nanocluster average diameter decreased with dose. Although this was observed in part from 0 to 1 dpa; by 25 dpa, the diameter was the same or higher for dispersoids. Second, the number density for nanoclusters increased whereas the dispersoid number density increased from 0 to 1 dpa, but then substantially decreased by 25 dpa. The lack of nanoclusters in APT relative to the dispersoids observed in STEM is attributed to the much larger analyzed volume of 200 nm×150 nm×~10 μm.

4 Discussion

4.1 Co-evolution of microstructure

The overall changes in microstructure are best assessed using sink strengths. The sink strength for the dislocation network is simply the network line density reported in Table 3. The sink strength of the dislocation loops was calculated using the following equation:

$$k_{loop}^2 = \pi \sum_{i=0}^{D} d_i \rho_i \quad (2)$$

where d_i is the dislocation loop diameter, ρ_i is the number density of loops of diameter d_i and D is the largest diameter size class. The precipitate sink strength is given by k_{prec}^2,

$$k_{prec}^2 = 2\pi \sum_{i=0}^{D} d_i N_i, \quad (3)$$

where d_i is the diameter of the dispersoid and N_i is the number density of dispersoids of diameter d_i.

The predicted sink strengths for each microstructure feature described in Equations (2) and (3) for the BM and SZ are plotted in Figure 11. Regardless of irradiation temperature or whether the material was welded, the dispersoid sink strength was higher in material irradiated to 1 dpa than to 25 dpa, except for the SZ at 500°C. Across temperature, the sink strength tended to be fairly consistent, with the highest values occurring at 450°C, 1 dpa: 1.41×10^{14} m^{-2} and 0.74×10^{14} m^{-2} for BM and SZ, respectively. The sink strength for loops (blue crossed) and the network (green hatched) is expressed as loop and network line length, respectively, and are also plotted in Figure 11. Overall, combined loop and network sink strength are higher than dispersoid sink strength for any given experimental conditions, except at 500°C, 1dpa where dispersoid sink strength was larger than the loop sink strength for both BM and SZ. There was no consistent trend of whether the dislocation sink strengths were larger for BM than the SZ.

In contrast, the sink strength for the nanoclusters in the base material was calculated using the diameter and number density determined from APT in Table 4. For the as received BM, the nanocluster sink strength was 3.73×10^{15} m^{-2}. At 25 dpa, the sink strengths were 68.4×10^{14} m^{-2}, 75.6×10^{14} m^{-2} and 99.4×10^{14} m^{-2}. All of these are an order of magnitude higher than the dispersoid or dislocation sink strengths reported in Figure 11 indicating that the dominant microstructure behavior in terms of sink strength is that of the nanoclusters. However, there were no nanoclusters observed via APT in the SZ, even though analyzed tip volumes were similar. The lack of nanoclusters would greatly impact the SZ hardening as a result. Since nanoclusters may form or dissolve in a dynamic fashion [70], this is a critical difference between the BM and SZ.

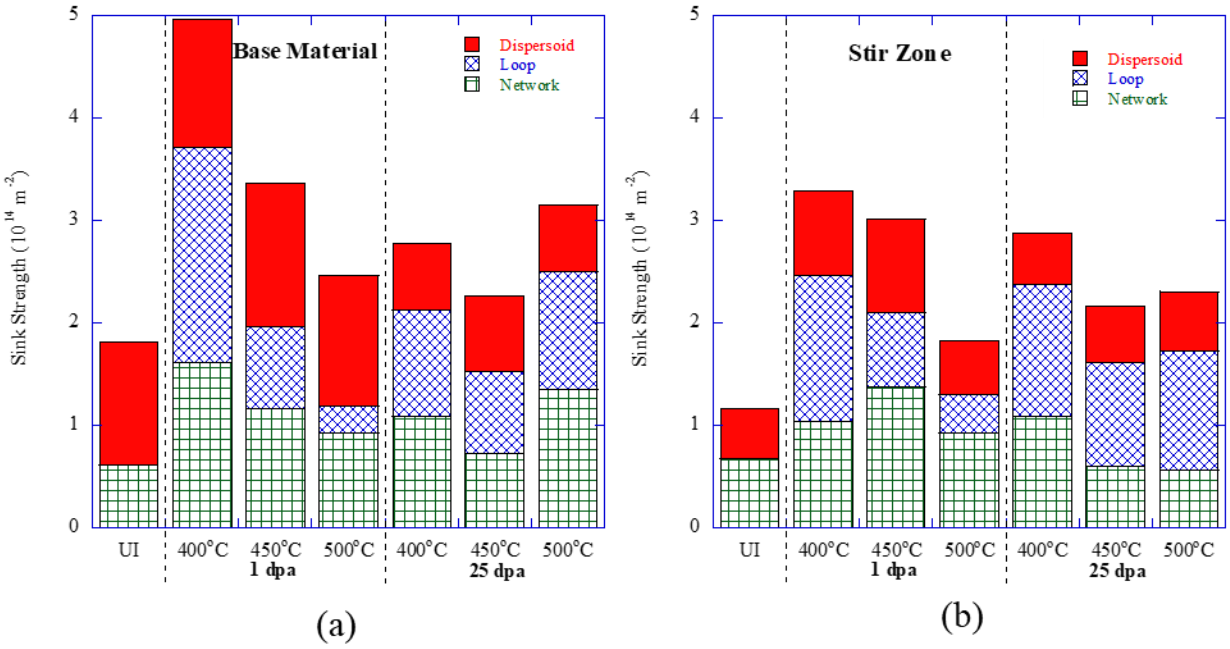

Figure 11: Evolution of dispersoid, loop, and network sink strength for a) BM and b) SZ in MA956 irradiated with 5 MeV Fe^{++} at 1 and 25 dpa at temperatures of 400, 450 [22], and 500°C. All data was taken in the 500 to 700 nm depth region via STEM imaging.

Ultimately the co-evolution of the microstructure, including nanoclusters and resulting solutes, should cause the resulting changes in mechanical properties noted in Figure 1. Considering the BM

microstructure, the overall trend is toward coarsening of dispersoid and dislocation loop morphology, while the dislocation network is the least dynamic and more or less remains within error bars after a small but expected increase with irradiation (Figure 7c). Despite the apparent softening observed, the overall sink strength tended to increase with irradiation initially then decrease. In particular, the sudden nucleation of loops as a category would normally suggest hardening consistent with other results for similar alloys [71–73], but this was not observed.

For the SZ, the initial sink strength greatly increased with the addition of any amount of irradiation due to appearance of loops, but additional dispersoids were nucleated as well. Since no nanoclustering was observed in the analyzed tip volumes, the lower sink strength is consistent with the lower yield stress observed both in unirradiated and irradiated cases for which there was data. Overall, the nanoclusters provided a significant source of sink strength and any dissolution or growth would likely be highly influential in the changes in the mechanical properties more so than larger, less abundant features such as the loops and dispersoids.

4.2 Correlation between Microstructure and Mechanical Properties

For evaluation of the strengthening mechanisms in the samples considered in this study, three separate mechanisms must be considered: a) grain size strengthening, b) solid solution strengthening, and c) dispersed barrier hardening (DBH). Grain size strengthening is primarily relevant for comparison of the BM and SZ where the average grain sizes differ by an order of magnitude. Solid solution strengthening is a potential contributor given the apparent migration of solutes from the nanoclusters to the matrix (as measured by APT) in the irradiated specimens. Dispersed barrier hardening will influence strengthening due to the presence of multiple inherent barriers to dislocation motion including larger STEM-visible dispersoids, smaller APT-detectable nanoclusters, and irradiation-induced dislocation loops.

When considering multiple mechanisms of strengthening, a common approach is to simply combine the individual effects linearly, particularly when dissimilar mechanisms are present [74]. Another approach for superimposing different features which contribute to DBH is via the root-sum-square (RSS) method. This latter approach has been shown to potentially be more effective at estimating the DBH contributions of different barrier types in at least one prior study of a model Fe-9%Cr ODS material [75]. For the purpose of this analysis, the RSS approach for the DBH contributing features was used and solid solution and grain size contributions were added linearly. A parallel analysis using a straight linear superposition was also conducted for this study, yielding similar results with just slightly lower strengthening contributions estimated for each barrier. For the RSS approach, the total increase in yield strength ($\Delta\sigma_y$) can be expressed as:

$$\Delta\sigma_y = \sqrt{\Delta\sigma_{disp}^2 + \Delta\sigma_{loop}^2 + \Delta\sigma_{nc}^2} + \Delta\sigma_{ss} + \Delta\sigma_{gs} \quad (4)$$

where $\Delta\sigma_{disp}$, $\Delta\sigma_{loop}$, $\Delta\sigma_{nc}$, $\Delta\sigma_{ss}$, and $\Delta\sigma_{gs}$ are the individual contributions to the change in yield strength for dispersoids, dislocation loops, nanoclusters, solid solution, and grain sizes, respectively.

The approach taken in this discussion will be to compare different sub-sets of samples to enable isolation of each mechanism for evaluation. Phase I will compare the strengthening between the unirradiated BM and SZ specimens to evaluate the effects of the friction stir welding process on the microstructure and resulting mechanical properties. Next, Phase II will evaluate the effects of irradiation temperature via comparison of common irradiation doses (25 dpa) at 400°C and 500°C, respectively, for both the BM and SZ specimens. Finally, Phase III will consider irradiation dose effects between 1 dpa and 25 dpa, although limited data is available at 1 dpa to conduct a full systematic analysis.

4.2.1 Phase I: Base Metal and Stir Zone Comparison

The MA956 BM and SZ microstructures differ in three primary ways: 1) grain size, 2) concentration of oxide-forming solutes (Y, Ti, and O) dissolved in solid solution, and 3) the presence of oxide nanoclusters. As a result, these differences are expected to be responsible for the differences in hardness and yield strength between the BM and SZ samples from the unirradiated and commonly irradiated specimens.

The strengthening effects of the grain sizes may be estimated using the Hall-Petch relationship [76,77]. Baker et al. previously evaluated the grain size strengthening in unirradiated MA956 (this alloy) [12], with their data yielding an estimated Hall-Petch relationship of:

$$\Delta\sigma_{gs} = 5.0d^{-1/2} + 485 \text{ (MPa)} \quad (5)$$

in which d is the average effective diameter (in mm) for the grains. Using the grain sizes found for this study (where the average grain diameter in the BM and SZ are 0.89 μm and 12.5 μm, respectively) the BM is estimated to be have a yield strength $\Delta\sigma_{gs}$ ~125 MPa higher due to grain size strengthening.

For estimating the effects of solid solution strengthening, a simple model is used to characterize the respective contribution of each solute species ($\Delta\sigma_{ss,i}$) in a bcc Fe matrix [78,79]:

$$\Delta\sigma_{ss,i} = K_i C_i \quad (6)$$

in which K_i is the solute-specific strengthening coefficient and C_i is the matrix composition of solute i. The strengthening effects of each solute may be subsequently added linearly [78] to estimate an overall solid solution strengthening impact from multiple solutes. Values for K_i vary for different solutes and have been estimated previously in [80] for solutes in bcc Fe. Generally, substitutional solutes such as Cr, Si, Mn, Ni, Mo, and Ti have been found to have K_i values ranging from 2 to 55 MPa/at%, suggesting that small compositional changes in these solutes will have very little influence on the strengthening of the bulk material. In this case of this study, substitutional solutes Ti and Y were estimated to have a similar value for K_i of ~20 MPa/at% (Table 6). Interstitial solutes have much higher K_i values, exceeding 1000 MPa/at% [75,78], and K_O was estimated to be ~1000 MPa/at% due to their likelihood of occupying interstitial sites when in solution. Table 6 provides an estimate of the relative solid solution strengthening effects for each of the oxide forming solutes (Y, Ti, O), which demonstrate measurable difference in matrix composition following each irradiation condition. Shown in Table 6, only the interstitial O solutes contribute substantial strengthening ranging from $\Delta\sigma_{ss}$ ~132 to 262 MPa in the BM and $\Delta\sigma_{ss}$ ~70 to 110 MPa in the SZ.

Table 6: Estimated solid solution strengthening effects determined from matrix compositions in Table 4 and Table 5 with Eq. (5).

Solute, *i*	Strengthening Coefficient, *K* (MPa/at%)	$\Delta\sigma_{ss}$ (MPa) in Base Metal (BM)				$\Delta\sigma_{ss}$ (MPa) in Stir Zone (SZ)			
		Unirrad.	25 dpa 400°C	25 dpa, 450°C	25 dpa, 500°C	Unirrad.	25 dpa 400°C	25 dpa, 450°C	25 dpa, 500°C
Cr	3 [78]	58	59	53	58	59	57	55	59
Al	9 [78]	78	74	75	75	77	74	73	77
Y	20 [75]	1	2	2	2	0	0	0	0
Ti	20 [78]	1	2	2	1	1	1	2	1
O	1000 [75]	132	256	262	219	70	86	110	86
Total (MPa)	-	271	394	393	355	207	218	239	222
Strengthening - above SZ (MPa)	-	64	176	154	133	-	-	-	-

Finally, the dispersed barrier hardening model may be used to relate discrete microstructural features to changes in the yield strength of the material using:

$$\Delta\sigma_{y,j} = \alpha_j M \mu b \sqrt{N_j d_j} \tag{7}$$

In this expression, M is the Taylor factor (3.06 for bcc Fe alloys [60]), μ is the shear modulus (82 GPa [74]), b is the Burgers vector magnitude (0.248 nm [74]), N_j is the number density of feature j, and d_j is the average diameter of feature j. The remaining factor (α_j) represents the relative strength of the barrier and is typically a coefficient between 0 and 1.

The analysis of the two unirradiated specimens (BM and SZ) consider only pre-existing dispersoids and nanoclusters. For the low-density dispersoids, a value for α_{disp} may be estimated using size- and density-dependent expressions developed by Tan and Busby for incoherent precipitates [81]:

$$\alpha_{disp}^{incoh} = \frac{0.135}{(1-\nu)^{1/2}\left(1-0.816\boldsymbol{d}\sqrt{\boldsymbol{Nd}}\right)} ln\left(\frac{0.816\boldsymbol{d}}{r_0}\right) \tag{8}$$

where ν is Poisson's ratio (~0.33), and r_0 is the dislocation core radius (estimated to equal to b). Although the extent of the coherency of the dispersoids is unknown and likely size dependent based upon other studies [82], this approach enables estimation of their contribution to strengthening. Using Eq. 8, the estimated values for α_{disp} range 0.60 to 0.71 for the unirradiated samples and provide strengthening estimates from Eq. 7 ($\Delta\sigma_{disp}$) of 115 MPa and 88 MPa for the unirradiated BM and SZ, respectively. On the other hand, this equation will likely not apply for the higher number density nanoclusters, as Eq. 8 estimates α_{nc} = 0.59 and strengthening ($\Delta\sigma_{nc}$) of 631 MPa for the BM, which far exceeds the measured yield strength difference of ~300 MPa above the unirradiated SZ specimen. A prior study of a model ODS [75] also suggests that smaller oxide nanoclusters may be more coherent with smaller values for α_{nc}. Instead, Eq. 4 is applied for both the unirradiated BM and SZ microstructures. Using the difference between these two expressions, the estimated value of α_{nc} = 0.15 was solved for directly. Thus, a summation of the strengthening contributions for the unirradiated BM and SZ are illustrated in Figure 12a for comparison to the measured difference in strengthening via microindentation (~300 MPa).

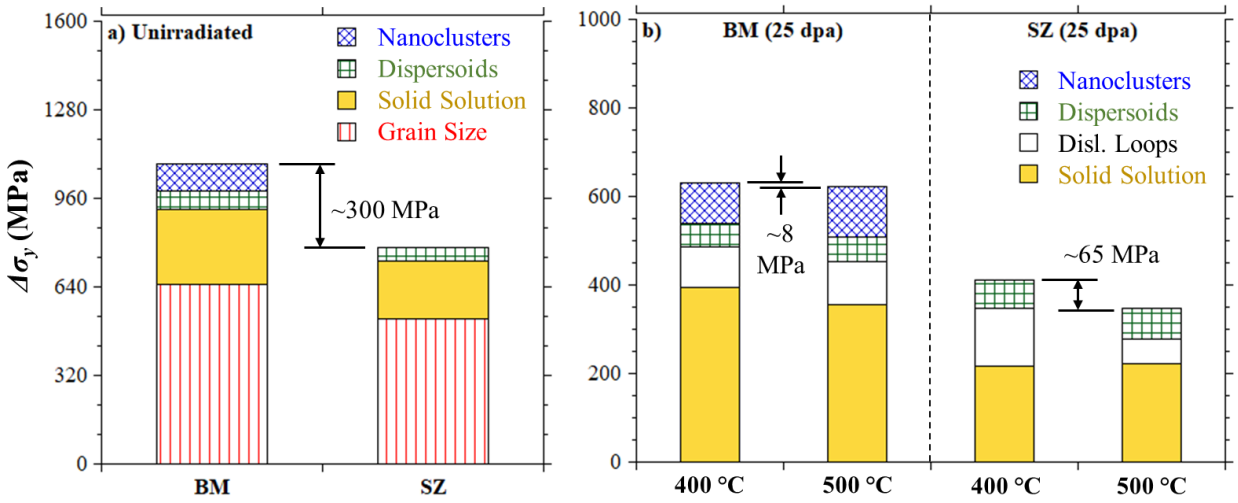

Figure 12: Estimated combined effects of strengthening mechanisms using Eq. 4 in a) unirradiated BM and SZ, and b) irradiated BM and SZ to 25 dpa, for irradiation temperatures of 400°C and 500°C. For the unirradiated specimens, the ~300 MPa change in strength is derived from the Vickers hardness results. For the irradiated specimens, the change in strength is derived from nanohardness results at each respective temperature.

4.2.2 Phase II: Irradiation Temperature Effects

To isolate the effects of irradiation temperature, the hardness and microstructure measurements are compared for the irradiations at 400°C and 500°C to 25 dpa in both the BM and SZ specimens. When irradiated to 25 dpa at 400°C, the BM is measured to have a nanohardness 0.03 GPa higher than following irradiation at 500°C, translating into a slightly higher yield strength by ~8 MPa. After each irradiation, both BM samples have similar irradiation-induced microstructures including dispersoids, nanoclusters, and dislocation loops. Similarly, in the SZ nanohardness following irradiation at 400°C is measured to be 0.22 GPa higher than after irradiation at 500°C, equating to a ~65 MPa higher yield strength. The SZ samples also have similar irradiation-induced microstructures with dispersoids and dislocation loops. The explanation for higher hardness following 400°C irradiation is likely due to two combined influences: 1) lower irradiation temperature results in slightly finer morphologies of dispersoids and loops (and nanoclusters in the BM specimens), and 2) increased concentrations of oxide solutes (including O) in the matrix due to partial irradiation-induced dissolution of the oxides.

For correlating the observed microstructures with the measured mechanical properties, Eq. 4 was again applied for the irradiations to 25 dpa at 400°C and 500°C, and the difference between the equations for each irradiation temperature to mathematically represent the measured differences in $\Delta\sigma_y$. With this approach, separate equations for the BM and SZ were written isolating three unknown values for α_{disp}, α_{loop}, and α_{nc}. Estimated values for α_{disp} may be approximated using Eq. 8 again for each measured morphology of dispersoids. Calculated values for α_{disp} are found to range from 0.60 to 0.73 (Table 7), which reduces the system of two equations to only include two unknowns that are directly solvable. Through solving these two equations for the differences in $\Delta\sigma_y$ within both BM and SZ, a value for α_{loop} = 0.60 is estimated. An alternative method use a similar size- and density-dependent expression developed by Tan and Busby for dislocation loops [81]:

$$\alpha_{loop} = \frac{0.271A}{(1-\nu)^{1/2}\sqrt{Nd}(16-\pi tA)} ln\left(\frac{0.637d}{r_0}\right) \quad (9)$$

where $a = \sqrt{16\pi Nd} + 4Nd^2 - \pi^2 Ndt$, and t is the dislocation loop thickness (0.165 nm for [111] loops in bcc Fe). Using the same approximation of r_0 = 0.248 nm, estimated values for α_{loop} using Eq. 9 range from 0.57 to 0.67 and are very similar to the fitted value of 0.60. Using the values from Eq. 8 for dispersoids and α_{loop} = 0.60, a value for α_{nc} = 0.11 is determined via the system of equations and is similar to the value found in phase I, shown in Figure 12b, further suggesting that the smaller-scale, APT-visible nanoclusters are likely more coherent with the surrounding matrix.

Table 7: Summary of dispersed strengthening hardening strengthening coefficients estimated from this study. (N.A. indicates that insufficient data is available to determine this parameter)

Strengthening coefficient	α_{disp}	α_{nc}	α_{loop}
Phase I			
Unirradiated BM	0.60	0.15	-
Unirradiated SZ	0.71	0.15	-
Phase II			
BM, 25 dpa, 400°C	0.60	0.11	0.67
BM, 25 dpa, 500°C	0.69	0.11	0.60
SZ, 25 dpa, 400°C	0.69	-	0.57
SZ, 25 dpa, 500°C	0.80	-	0.62
Phase III			
BM, 1 dpa, 400°C	0.55	N.A.	0.48
BM, 1 dpa, 500°C	0.59	N.A.	0.60
SZ, 1 dpa, 400°C	0.72	-	0.53
SZ, 1 dpa, 500°C	0.75	-	0.61

4.2.3 Phase III: Irradiation Dose Effects

For evaluation of the dose effects on microstructure and mechanical properties, the hardness and microstructure measurements were compared from 1 dpa and 25 dpa at irradiation temperatures of 400°C and 500°C in the BM and SZ samples. Upon irradiation to 400°C, the BM specimens at 1 dpa have a nanohardness that is 0.14 GPa higher than after longer irradiation to 25 dpa, equating to ~42 MPa higher yield strength. Similarly, upon irradiation at 500°C, the BM specimens are also 0.17 GPa harder at 1 dpa than they are after 25 dpa, translating to a difference of ~48 MPa in yield strength. Meanwhile, the SZ specimens follow a similar pattern. Upon 400°C irradiation, the 1 dpa samples are 0.30 GPa harder than at 25 dpa, equating to ~88 MPa in higher yield strength. At 500°C, the 1 dpa samples are 0.23 GPa harder (~68 MPa) than those irradiated to 25 dpa.

For correlation between microstructure and yield strength, a similar approach was applied to estimate the values for α_{disp} and α_{loop} using Eq. 8 and Eq. 9 for dispersoids and dislocation loops observed via STEM following each 1 dpa irradiation. The results of these calculations are presented in for comparison with their counterparts following 25 dpa irradiation at the same temperatures. In most cases, the size- and density-dependent values for α_{disp} and α_{loop} are slightly lower following 1 dpa than they are after 25 dpa of irradiation. This simple comparison suggests that the dispersed barrier hardening due to dispersoids and loops is not expected to be substantial higher in the 1 dpa samples compared to the 25 dpa samples. In fact, the estimated hardening of the SZ samples using Eq. 4 and taking the difference between the 1 dpa and 25 dpa samples at each irradiation temperature yields much lower predicted hardening (~12 MPa and 7 MPa for 400°C and 500°C, respectively) than is measured via nanoindentation (88 MPa and 68 MPa, respectively). This discrepancy suggests that an additional hardening mechanism such as solid solution strengthening is also present. If this is the case, it would suggest that low dose irradiation at 1 dpa results in partial dissolution via ballistic solution of pre-existing dispersoids into solid solution, resulting in a partial increase in concentration of oxide solutes (including O) that strengthen the material. Ballistic dissolution and radiation enhanced diffusion are two competing mechanisms affecting the stability of dispersoids or nanoprecipitates, and it is well-documented that the dominance of one mechanisms over the other is highly dependent on temperature, dose, and sink strength [6,62,63,83,84]. The subsequent softening occurring after 25 dpa irradiation implies that these solutes potentially segregate toward more stable dispersoids at

higher dose, and combine with observed coarsening of the dispersoids and dislocation loops to result in a slightly lower hardness and yield strength at the higher dose. Unfortunately, a full suite of APT-based data was not available to characterize the solute concentrations in the matrix at the lower dose levels to confirm this hypothesis. A similar comparison could be extracted for the BM samples. Without considering any nanoclusters or solid solution strengthening, the yield strength of the BM (using Eq. 4) following 1 dpa irradiation is predicted to be ~14 MPa higher than 25 dpa at 400°C, and the 1 dpa sample is actually estimated to be softer (-46 MPa) than the 25 dpa specimen at the 500°C temperature. This comparison suggests that dispersed hardening due to nanoclusters and solid solution strengthening due to oxide solutes are likely to be additional contributors to the strengthening mechanisms.

5 Conclusions

- ODS MA956 was friction stir welded then ion irradiated with 5 MeV Fe^{++} at 400, 450 and 500°C. After welding and irradiation, the mechanical properties were assessed with nanoindentation and the microstructure was assessed with scanning transmission electron microscopy and atom probe tomography to determine the combined effect of welding and irradiation.
- The process of friction stir welding in MA956 results in stir zone material with yield strength that decreased ~300 MPa relative to the base material, regardless of irradiation conditions. The softer stir zone is likely due to increased grain sizes, redistribution of oxide nanoclusters, and lower levels of oxide-forming solutes within solution. The dominant effect on both the microstructure and mechanical properties was due to welding process rather than irradiation.
- The dispersoids in the base material tended to coarsen with irradiation. The formation of new dispersoids as a result of irradiation in the stir zone was also observed, though there was also modest growth in the average dispersoid diameter. With increased temperature, a lower number density of larger dispersoids was observed. Loops formed at all temperatures and promoted a finer morphology at the lowest temperature of 400°C. Although the evolution of the dislocation loops was inconsistent, the loop diameter tended to increase with temperature and increased less strongly with dose. The number density decreased with temperature and the network density was mostly stable. Nanoclusters were observed via APT in the base material only.
- Irradiation at the lowest temperature of 400°C resulted in slightly higher strength than irradiation at 500°C to the same doses in both the BM and SZ. This is attributed to lower irradiation temperature promoting finer morphologies of dispersoids and loops (and nanoclusters in the BM specimens), and 2) increased concentrations of oxide solutes (including O) in the matrix due to partial irradiation-induced dissolution of the oxides.
- Low dose irradiation at 1 dpa likely resulted in partial dissolution of some pre-existing dispersoids into solid solution, resulting is a partial increase in concentration of oxide solutes (including O) that strengthen the material. The subsequent softening occurring at 25 dpa implies that these solutes potentially re-coalesce into dispersoids at higher dose, and combine with observed coarsening of the dispersoids and dislocation loops to result in a slightly lower hardness and yield strength at the higher dose.

6 Acknowledgements

The authors gratefully acknowledge Dan Buller for assistance in ion irradiation and thank Tim Tilton and Nick Brubaker at the University of Idaho for Vickers hardness testing. The authors also recognize Y. Wu in the Microscopy and Characterization Suite (MaCS) at the Center for Advanced Energy Studies (CAES) for generously enabling utilization of a remote access computer for APT data analysis. Research Supported by the Defense Threat Reduction Agency (DTRA) through grant HDTRA113691. This research was supported by Army Research Laboratories Aberdeen through the Open Campus program. This work was performed, in part, at the Center for Integrated Nanotechnologies, an Office of Science User Facility operated for the U.S. Department of Energy (DOE) Office of Science. Sandia National Laboratories is a multi-mission laboratory managed and operated by National Technology and Engineering Solutions of Sandia, LLC. a wholly owned subsidiary of Honeywell International, Inc., for the U.S. Department of Energy's National Nuclear Security Administration under contract DE-NA-0003525. This paper describes objective technical results and analysis. Any subjective views or opinions that might be expressed in the paper do not necessarily represent the views of the U.S. Department of Energy, Department of Defense or the United States Government.

7 References

[1] Nuscale Power LLC, NuScale Standard Plant, Design Certification Application, Reactor, (2016).

[2] G.S. Was, Z. Jiao, E. Getto, K. Sun, A.M. Monterrosa, S.A. Maloy, O. Anderoglu, B.H. Sencer, M. Hackett, Emulation of reactor irradiation damage using ion beams, Scr. Mater. 88 (2014) 33–36. https://doi.org/10.1016/j.scriptamat.2014.06.003.

[3] Z. Jiao, S. Taller, K.G. Field, G. Yeli, M.P. Moody, G.S. Was, Microstructure evolution of T91 irradiated in the BOR60 fast reactor, J. Nucl. Mater. 504 (2018) 122–134.

[4] M.B. Toloczko, F.A. Garner, V.N. Voyevodin, V.V. Bryk, O.V. Borodin, V.V. Mel'nychenko, A.S. Kalchenko, Ion-induced swelling of ODS ferritic alloy MA957 tubing to 500 dpa, J. Nucl. Mater. 453 (2014) 323–333. https://doi.org/10.1016/j.jnucmat.2014.06.011.

[5] ASTM E8-04, Standard Test Methods for Tension Testing of Metallic Materials, in: Annu. B. ASTM Stand., 2007: pp. 1–27. https://doi.org/10.1520/E0008.

[6] E. Getto, N. Nathan, J. McMahan, B. Baker, S. Taller, Contextualizing dispersoid evolution within the microstructure of MA956 using ion irradiation, Nucl. Mater. Energy. 28 (2021) 101024. https://doi.org/10.1016/j.nme.2021.101024.

[7] D.S. Gelles, Microstructural examination of commercial ferritic alloys at 200 dpa, J. Nucl. Mater. 233–237 (1996) 293–298. https://doi.org/10.1016/S0022-3115(96)00222-X.

[8] T. Chen, H. Kim, J.G. Gigax, D. Chen, C.C. Wei, F.A. Garner, L. Shao, Radiation response of oxide-dispersion-strengthened alloy MA956 after self-ion irradiation, Nucl. Instruments Methods Phys. Res. Sect. B Beam Interact. with Mater. Atoms. 409 (2017) 259–263. https://doi.org/10.1016/j.nimb.2017.05.024.

[9] M.G. McKimpson, D.O. Donnell, Joining ODS Materials For High. Temperature Applications, JOM. 957 (1994) 956–958.

[10] B.W. Baker, E.S.K. Menon, T.R. McNelley, L.N. Brewer, B. El-Dasher, J.C. Farmer, S.G. Torres, M.W. Mahoney, S. Sanderson, Processing-Microstructure Relationships in Friction Stir Welding of MA956 Oxide Dispersion Strengthened Steel, Metall. Mater. Trans. E. 1 (2014) 318–330. https://doi.org/10.1007/s40553-014-0033-6.

[11] B.W. Baker, T.R. McNelley, L.N. Brewer, Grain size and particle dispersion effects on the tensile behavior of friction stir welded MA956 oxide dispersion strengthened steel from low to elevated temperatures, Mater. Sci. Eng. A. 589 (2014) 217–227. https://doi.org/10.1016/j.msea.2013.09.092.

[12] B.W. Baker, K.E. Knipling, L.N. Brewer, Oxide Particle Growth During Friction Stir Welding of Fine Grain MA956 Oxide Dispersion Strengthened Steel, Metall. Mater. Trans. E. (2017) 1–12. https://doi.org/10.1007/s40553-016-0101-1.

[13] B.W. Baker, L.N. Brewer, Joining of Oxide Dispersion Strengthened Steels for Advanced Reactors, JOM. 66 (2014) 2442–2457. https://doi.org/10.1007/s11837-014-1206-6.

[14] Y.H. Guo, Y.Q. Chang, J. Zhang, J.Z. Li, S. Ukai, F.R. Wan, Microstructures and ion-irradiation behaviour of friction stir welded 12Cr-ODS steel, Sci. Technol. Weld. Join. 23 (2018) 50–57. https://doi.org/10.1080/13621718.2017.1392075.

[15] C.L. Chen, A. Richter, R. Kögler, M. Griepentrog, P. Reinstädt, Ion-irradiation effects on dissimilar friction stir welded joints between ODS alloy and ferritic stainless steel, J. Alloys Compd. 615 (2015) S448–S453. https://doi.org/10.1016/j.jallcom.2013.11.123.

[16] C.L. Chen, G.J. Tatlock, A.R. Jones, Microstructural evolution in friction stir welding of nanostructured ODS alloys, J. Alloys Compd. 504 (2010) S460–S466. https://doi.org/10.1016/j.jallcom.2010.02.192.

[17] J. Wang, W. Yuan, R.S. Mishra, I. Charit, Microstructure and mechanical properties of friction stir welded oxide dispersion strengthened alloy, J. Nucl. Mater. 432 (2013) 274–280. https://doi.org/10.1016/j.jnucmat.2012.08.001.

[18] Z. Yu, Z. Feng, D. Hoelzer, L. Tan, M.A. Sokolov, Friction Stir Welding of ODS and RAFM Steels, Metall. Mater. Trans. E. 2 (2015) 164–172. https://doi.org/10.1007/s40553-015-0054-9.

[19] W. Han, P. Liu, X. Yi, Q. Zhan, F. Wan, K. Yabuuchi, H. Serizawa, A. Kimura, Impact of friction stir welding on recrystallization of oxide dispersion strengthened ferritic steel, J. Mater. Sci. Technol. (2017). https://doi.org/10.1016/j.jmst.2017.11.032.

[20] B. Mazumder, X. Yu, P.D. Edmondson, C.M. Parish, M.K. Miller, H.M. Meyer, Z. Feng, Effect of friction stir welding and post-weld heat treatment on a nanostructured ferritic alloy, J. Nucl. Mater. 469 (2016) 200–208. https://doi.org/10.1016/j.jnucmat.2015.11.061.

[21] J.P. Wharry, M.J. Swenson, K.H. Yano, A review of the irradiation evolution of dispersed oxide nanoparticles in the b.c.c. Fe-Cr system: Current understanding and future directions, J. Nucl. Mater. 486 (2017) 11–20. https://doi.org/10.1016/j.jnucmat.2017.01.009.

[22] E. Getto, B. Baker, B. Tobie, S. Briggs, K. Hattar, K. Knipling, Effect of friction stir welding and self-ion irradiation on dispersoid evolution in oxide dispersion strengthened steel MA956 up to 25 dpa, J. Nucl. Mater. 515 (2019) 407–419. https://doi.org/10.1016/j.jnucmat.2018.12.040.

[23] E. Getto, N. Nathan, J. McMahan, S. Taller, B. Baker, Understanding radiation effects in friction stir welded MA956 using ion irradiation and a rate theory model, J. Nucl. Mater. 561 (2022) 153530. https://doi.org/10.1016/j.jnucmat.2022.153530.

[24] B.W. Baker, Processing, Microstructure, and Material Property Relationships Following Friction Stir Welding of Oxide Dispersion Strengthened Steels, (2010).

[25] J.F. Ziegler, M.D. Ziegler, J.P. Biersack, SRIM – The stopping and range of ions in matter (2010), Nucl. Instruments Methods Phys. Res. Sect. B Beam Interact. with Mater. Atoms. 268 (2010) 1818–1823. https://doi.org/10.1016/j.nimb.2010.02.091.

[26] W.C. Oliver, G.M. Pharr, An improved technique for determining hardness and elastic modulus using load and displacement sensing indentation experiments, J. Mater. Res. 7 (1992) 1564–1583.

[27] Y.F. Jia, Y.Y. Cui, F.Z. Xuan, F. Yang, Comparison between single loading-unloading indentation and continuous stiffness indentation, RSC Adv. 7 (2017) 35655–35665. https://doi.org/10.1039/c7ra06491h.

[28] P. Haušild, Methodological comment on the nanoindentation of ion-irradiation hardened materials, J. Nucl. Mater. 551 (2021) 152987. https://doi.org/10.1016/j.jnucmat.2021.152987.

[29] P. Hosemann, D. Kiener, Y. Wang, S.A. Maloy, Issues to consider using nano indentation on shallow ion beam irradiated materials, J. Nucl. Mater. 425 (2012) 136–139.

https://doi.org/10.1016/j.jnucmat.2011.11.070.

[30] S.S. Chiang, D.B. Marshall, A.G. Evans, The response of solids to elastic/plastic indentation. I. Stresses and residual stresses, J. Appl. Phys. 53 (1982) 298–311. https://doi.org/10.1063/1.329930.

[31] M. Yoshioka, Plastically deformed region around indentations on Si single crystal, J. Appl. Phys. 76 (1994) 7790–7796. https://doi.org/10.1063/1.357957.

[32] H. Huang, D. Bahr, J. Nelson, D. Kramer, M. Kriese, A. Wright, J. Robach, W.W. Gerberich, Yield strength predictions from the plastic zone around nanocontacts, Acta Mater. 47 (1998) 333–343.

[33] C.K. Dolph, D.J. da Silva, M.J. Swenson, J.P. Wharry, Plastic zone size for nanoindentation of irradiated Fe—9%Cr ODS, J. Nucl. Mater. 481 (2016) 33–45. https://doi.org/10.1016/j.jnucmat.2016.08.033.

[34] Z. Huang, A. Harris, S.A. Maloy, P. Hosemann, Nanoindentation creep study on an ion beam irradiated oxide dispersion strengthened alloy, J. Nucl. Mater. 451 (2014) 162–167. https://doi.org/10.1016/j.jnucmat.2014.03.036.

[35] L.A. Giannuzzi, J.L. Drown, S.R. Brown, R.B. Irwin, F.. Stevie, Applications of the FIB lift-out technique for TEM specimen preparation, Microsc Res Tech. 41 (1998) 285–290. https://doi.org/10.1055/s-0033-1341065.

[36] T. Malis, S.C. Cheng, R.F. Egerton, EELS log-ratio technique for specimen-thickness measurement in the TEM, J. Electron Microsc. Tech. 193–200 (1988).

[37] E. Getto, Z. Jiao, A.M. Monterrosa, K. Sun, G.S. Was, Effect of pre-implanted helium on void swelling evolution in self-ion irradiated HT9, J. Nucl. Mater. 462 (2015) 458–469. https://doi.org/10.1016/j.jnucmat.2015.01.045.

[38] C.M. Parish, K.G. Field, A.G. Certain, J.P. Wharry, Application of STEM characterization for investigating radiation effects in BCC Fe-based alloys, J. Mater. Res. 30 (2015) 1275–1289. https://doi.org/10.1557/jmr.2015.32.

[39] K. Thompson, D. Lawrence, D.J. Larson, J.D. Olson, T.F. Kelly, B. Gorman, In situ site-specific specimen preparation for atom probe tomography, Ultramicroscopy. 107 (2007) 131–139. https://doi.org/10.1016/j.ultramic.2006.06.008.

[40] M.K. Miller, K.F. Russell, K. Thompson, R. Alvis, D.J. Larson, Review of atom probe FIB-Based specimen preparation methods, Microsc. Microanal. 13 (2007) 428–436.

[41] J.Y. Lee, J.-P. Ahn, Specimen Preparation for Atom Probe Tomography, Appl. Microsc. 46 (2016) 14–19.

[42] T.J. Prosa, D.J. Larson, Modern Focused-Ion-Beam-Based Site-Specific Specimen Preparation for Atom Probe Tomography, Microsc. Microanal. 23 (2017) 194–209.

[43] J.M. Hyde, E.A. Marquis, K.B. Wilford, T.J. Williams, A sensitivity analysis of the maximum separation method for the characterisation of solute clusters, Ultramicroscopy. 111 (2011) 440–447. https://doi.org/10.1016/j.ultramic.2010.12.015.

[44] J. He, F. Wan, K. Sridharan, T.R. Allen, A. Certain, Y.Q. Wu, Response of 9Cr-ODS steel to proton irradiation at 400 °c, J. Nucl. Mater. 452 (2014) 87–94.

https://doi.org/10.1016/j.jnucmat.2014.05.004.

[45] J. He, F. Wan, K. Sridharan, T.R. Allen, A. Certain, V. Shutthanandan, Y.Q. Wu, Stability of nanoclusters in 14YWT oxide dispersion strengthened steel under heavy ion-irradiation by atom probe tomography, J. Nucl. Mater. 455 (2014) 41–45. https://doi.org/10.1016/j.jnucmat.2014.03.024.

[46] M.L. Lescoat, J. Ribis, Y. Chen, E.A. Marquis, E. Bordas, P. Trocellier, Y. Serruys, A. Gentils, O. Kaïtasov, Y. De Carlan, A. Legris, Radiation-induced Ostwald ripening in oxide dispersion strengthened ferritic steels irradiated at high ion dose, Acta Mater. 78 (2014) 328–340. https://doi.org/10.1016/j.actamat.2014.06.060.

[47] M.J. Swenson, J.P. Wharry, Nanocluster irradiation evolution in Fe-9%Cr ODS and ferritic-martensitic alloys, J. Nucl. Mater. 496 (2017) 24–40. https://doi.org/10.1016/j.jnucmat.2017.08.045.

[48] R.P. Kolli, D.N. Seidman, Comparison of compositional and morphological atom-probe tomography analyses for a multicomponent Fe-Cu steel, Microsc. Microanal. 13 (2007) 272–284. https://doi.org/10.1017/S1431927607070675.

[49] C.A. Williams, D. Haley, E.A. Marquis, G.D.W. Smith, M.P. Moody, Defining clusters in APT reconstructions of ODS steels, Ultramicroscopy. 132 (2013) 271–278. https://doi.org/10.1016/j.ultramic.2012.12.011.

[50] M.K. Miller, R.G. Forbes, Atom probe tomography, Mater. Charact. 60 (2009) 461–469. https://doi.org/10.1016/j.matchar.2009.02.007.

[51] C.A. Williams, E.A. Marquis, A. Cerezo, G.D.W. Smith, Nanoscale characterisation of ODS-Eurofer 97 steel: An atom-probe tomography study, J. Nucl. Mater. 400 (2010) 37–45. https://doi.org/10.1016/j.jnucmat.2010.02.007.

[52] C. Robertson, B.K. Panigrahi, S. Balaji, S. Kataria, Y. Serruys, M.H. Mathon, C.S. Sundar, Particle stability in model ODS steel irradiated up to 100 dpa at 600°C: TEM and nano-indentation investigation, J. Nucl. Mater. 426 (2012) 240–246. https://doi.org/10.1016/j.jnucmat.2012.04.001.

[53] P. Hosemann, E. Stergar, L. Peng, Y. Dai, S.A. Maloy, M.A. Pouchon, K. Shiba, D. Hamaguchi, H. Leitner, Macro and microscale mechanical testing and local electrode atom probe measurements of STIP irradiated F82H, Fe-8Cr ODS and Fe-8Cr-2W ODS, J. Nucl. Mater. 417 (2011) 274–278. https://doi.org/10.1016/j.jnucmat.2010.12.200.

[54] K. Vogel, C. Heintze, P. Chekhonin, S. Akhmadaliev, E. Altstadt, F. Bergner, Relationships between depth-resolved primary radiation damage, irradiation-induced nanostructure and nanoindentation response of ion-irradiated Fe-Cr and ODS Fe-Cr alloys, Nucl. Mater. Energy. 24 (2020) 100759. https://doi.org/10.1016/j.nme.2020.100759.

[55] B. Duan, C. Heintze, F. Bergner, A. Ulbricht, S. Akhmadaliev, E. Oñorbe, Y. de Carlan, T. Wang, The effect of the initial microstructure in terms of sink strength on the ion-irradiation-induced hardening of ODS alloys studied by nanoindentation, J. Nucl. Mater. 495 (2017) 118–127. https://doi.org/10.1016/j.jnucmat.2017.08.014.

[56] B.W. Baker, K.E. Knipling, L.N. Brewer, Oxide Particle Growth During Friction Stir Welding of Fine Grain MA956 Oxide Dispersion-Strengthened Steel, Metall. Mater. Trans. E. 4 (2017) 1–12. https://doi.org/10.1007/s40553-016-0101-1.

[57] M. West, B. Jasthi, P. Hosemann, V. Sodesetti, Friction Stir Welding of Oxide Dispersion Strengthened Alloy MA956, in: Frict. Stir Weld. Process. VI, 2011: pp. 33–40.

[58] V. Voyevodin, M. Tikhonovsky, G. Tolstolutska, H. Rostova, R. Vasilenko, O. Kalchenko, N. Andrievska, O. Velikodnyi, Structural features and operational characteristics of steel T91, East Eur. J. Phys. (2020). https://doi.org/10.26565/2312-4334-2020-3-12.

[59] S. Kang, Y.S. Jung, J.H. Jun, Y.K. Lee, Effects of recrystallization annealing temperature on carbide precipitation, microstructure, and mechanical properties in Fe-18Mn-0.6C-1.5Al TWIP steel, Mater. Sci. Eng. A. 527 (2010) 745–751. https://doi.org/10.1016/j.msea.2009.08.048.

[60] J.T. Busby, M.C. Hash, G.S. Was, The relationship between hardness and yield stress in irradiated austenitic and ferritic steels, J. Nucl. Mater. 336 (2005) 267–278. https://doi.org/10.1016/j.jnucmat.2004.09.024.

[61] A.C. Fischer-Cripps, Nanoindentation, Springer, New York, 2011.

[62] M.L. Lescoat, J. Ribis, Y. Chen, E.A. Marquis, E. Bordas, P. Trocellier, Y. Serruys, A. Gentils, O. Kaïtasov, Y. De Carlan, A. Legris, Radiation-induced Ostwald ripening in oxide dispersion strengthened ferritic steels irradiated at high ion dose, Acta Mater. 78 (2014) 328–340. https://doi.org/10.1016/j.actamat.2014.06.060.

[63] E. Aydogan, N. Almirall, G.R. Odette, S.A. Maloy, O. Anderoglu, L. Shao, J.G. Gigax, L. Price, D. Chen, T. Chen, F.A. Garner, Y. Wu, P. Wells, J.J. Lewandowski, D.T. Hoelzer, Stability of nanosized oxides in ferrite under extremely high dose self ion irradiations, J. Nucl. Mater. 486 (2017) 86–95. https://doi.org/10.1016/j.jnucmat.2017.01.015.

[64] R.L. Klueh, D.R. Harries, High-Chromium Ferritic and Martensitic Steels for Nuclear Applications, American Society for Testing and Measurement, West Conshohocken, PA, 2001. https://doi.org/10.1520/MONO3-EB.

[65] S. Taller, Z. Jiao, K. Field, G.S. Was, Emulation of fast reactor irradiated T91 using dual ion beam irradiation, J. Nucl. Mater. 527 (2019). https://doi.org/10.1016/j.jnucmat.2019.151831.

[66] E. Getto, K. Sun, A.M. Monterrosa, Z. Jiao, M.J. Hackett, G.S. Was, Void swelling and microstructure evolution at very high damage level in self-ion irradiated ferritic-martensitic steels, J. Nucl. Mater. 480 (2016) 159–176. https://doi.org/10.1016/j.jnucmat.2016.08.015.

[67] C.M. Parish, K.G. Field, A.G. Certain, J.P. Wharry, Application of STEM characterization for investigating radiation effects in BCC Fe-based alloys, J. Mater. Res. 30 (2015) 1275–1289. https://doi.org/10.1557/jmr.2015.32.

[68] E.R. Reese, N. Almirall, T. Yamamoto, S. Tumey, G. Robert Odette, E.A. Marquis, Dose rate dependence of Cr precipitation in an ion-irradiated Fe[sbnd]18Cr alloy, Scr. Mater. 146 (2018) 213–217. https://doi.org/10.1016/j.scriptamat.2017.11.040.

[69] J.H. Ke, E.R. Reese, E.A. Marquis, G.R. Odette, D. Morgan, Flux effects in precipitation under irradiation – Simulation of Fe-Cr alloys, Acta Mater. 164 (2019) 586–601. https://doi.org/10.1016/j.actamat.2018.10.063.

[70] M.J. Swenson, J.P. Wharry, The comparison of microstructure and nanocluster evolution in proton and neutron irradiated Fe-9%Cr ODS steel to 3 dpa at 500 °c, J. Nucl. Mater. 467 (2015) 97–112. https://doi.org/10.1016/j.jnucmat.2015.09.022.

[71] H. Zhang, C. Zhang, Y. Yang, Y. Meng, J. Jang, A. Kimura, Irradiation hardening of ODS ferritic steels under helium implantation and heavy-ion irradiation, J. Nucl. Mater. 455 (2014) 349–353. https://doi.org/10.1016/j.jnucmat.2014.06.062.

[72] J. Gao, P. Song, Y.J. Huang, K. Yabuuchi, A. Kimura, K. Sakamoto, S. Yamashita, Effects of neutron irradiation on 12Cr–6Al-ODS steel with electron-beam weld line, J. Nucl. Mater. 524 (2019) 1–8. https://doi.org/10.1016/j.jnucmat.2019.06.028.

[73] T. Yamamoto, G.R. Odette, H. Kishimoto, J.W. Rensman, P. Miao, On the effects of irradiation and helium on the yield stress changes and hardening and non-hardening embrittlement of ~8Cr tempered martensitic steels: Compilation and analysis of existing data, J. Nucl. Mater. 356 (2006) 27–49. https://doi.org/10.1016/j.jnucmat.2006.05.041.

[74] I. Kubena, B. Fournier, T. Kruml, Effect of microstructure on low cycle fatigue properties of ODS steels, J. Nucl. Mater. 424 (2012) 101–108. https://doi.org/10.1016/j.jnucmat.2012.02.011.

[75] M.J. Swenson, C.K. Dolph, J.P. Wharry, The effects of oxide evolution on mechanical properties in proton- and neutron-irradiated Fe-9%Cr ODS steel, J. Nucl. Mater. 479 (2016) 426–435. https://doi.org/10.1016/j.jnucmat.2016.07.022.

[76] W.D. Callister, Materials science and engineering : an introduction / William D. Callister, Jr., (2007). http://ezlibproxy1.ntu.edu.sg/login?url=http://search.ebscohost.com/login.aspx?direct=true&db=cat00103a&AN=ntu.a404833&site=eds-live&scope=site.

[77] C.R. Barrett, A.S. Tetelman, W.D. Nix, The Principles of Engineering Materials, 1973.

[78] Q. Lu, W. Xu, S. Van Der Zwaag, Designing new corrosion resistant ferritic heat resistant steel based on optimal solid solution strengthening and minimisation of undesirable microstructural components, Comput. Mater. Sci. 84 (2014) 198–205. https://doi.org/10.1016/j.commatsci.2013.12.009.

[79] F.B. Pickering, Physical Metallurgy and the Design of Steels, Appl. Sci. Publ. LTD. (1978).

[80] W.C. Leslie, Iron and Its Dilute Substitutional Solid-Solutions, Metall. Trans. 3 (1972) 5–26.

[81] L. Tan, J.T. Busby, Formulating the strength factor α for improved predictability of radiation hardening, J. Nucl. Mater. 465 (2015) 724–730. https://doi.org/10.1016/j.jnucmat.2015.07.009.

[82] T. Chen, J.G. Gigax, L. Price, D. Chen, S. Ukai, E. Aydogan, S.A. Maloy, F.A. Garner, L. Shao, Temperature dependent dispersoid stability in ion-irradiated ferritic-martensitic dual-phase oxide-dispersion-strengthened alloy: Coherent interfaces vs. incoherent interfaces, Acta Mater. 116 (2016) 29–42. https://doi.org/10.1016/j.actamat.2016.05.042.

[83] J. Ribis, M.L. Lescoat, Y. De Carlan, J.M. Costantini, I. Monnet, T. Cozzika, F. Delabrouille, J. Malaplate, Stability of nano-oxides upon heavy ion irradiation of an ODS material, J. Nucl. Mater. 417 (2011) 262–265. https://doi.org/10.1016/j.jnucmat.2010.12.068.

[84] H. Kim, J.G. Gigax, T. Chen, S. Ukai, F.A. Garner, L. Shao, Dispersoid stability in ion irradiated oxide-dispersion-strengthened alloy, J. Nucl. Mater. 509 (2018) 504–512.